

# Periodic changes in the morphology of the Galactic resonance rings

A.M. Melnik<sup>1\*</sup>, E.N. Podzolkova<sup>1,2</sup>, A.K. Dambis<sup>1</sup>,

<sup>1</sup>*Sternberg Astronomical Institute, Lomonosov Moscow State University, Universitetskii pr. 13, Moscow, 119991, Russia*

<sup>2</sup>*Faculty of Physics, Lomonosov Moscow State University, Leninskie Gory 1-2, Moscow, 119991, Russia*

Accepted 2023 December 00. Received 2022 December 00; in original form 2023 December 00

## ABSTRACT

We study the periodic enhancement of either trailing or leading segments of the resonance elliptical rings in the dynamical model of the Galaxy which reproduces distributions of observed velocities derived from *Gaia* DR3 (EDR3) data along the Galactocentric distance. The model disc forms a nuclear ring, an inner combined ring and outer resonance rings  $R_1$  and  $R_2$ . The backbone of the inner combined ring is banana-type orbits around the Lagrange equilibrium points  $L_4$  and  $L_5$ . Orbits associated with the unstable equilibrium points  $L_1$  and  $L_2$  also support the inner ring. We have found the changes of the morphology of the inner ring with a period of  $P = 0.57 \pm 0.02$  Gyr, which is close to the period of revolution along the long-period orbits around the points  $L_4$  and  $L_5$ . A possible explanation of these morphological changes is the formation of an overdensity which then begins circulating along the closed contour. In the region of the Outer Lindblad Resonance (OLR), we have found the changes of the morphology of the outer rings with a period of  $P = 2.0 \pm 0.1$  Gyr. Probably, the morphological changes of the outer rings are due to the orbits trapped by the OLR. These orbits exhibit librations of the direction of orbital elongation with respect to the minor axis of the bar as well as the long-term variations in the stellar angular momentum, energy, average radius of the orbit, and eccentricity. Among many librating orbits, we discovered orbits with the libration period of  $P = 1.91 \pm 0.01$  Gyr, which may cause the morphological changes of the outer rings.

**Key words:** Galaxy: kinematics and dynamics – Galaxies: bar – catalogues

## 1 INTRODUCTION

There is extensive evidence for the presence of the bar in our Galaxy (Dwek et al. 1995; Fux 2001; Mühlbauer & Dehnen 2003; Benjamin et al. 2005; Cabrera-Lavers et al. 2007; Churchwell et al. 2009; Gerhard 2011; González-Fernández et al. 2012; Ness & Lang 2016; Simion et al. 2017). Solid rotation of the bar in the differentially rotating disc causes the appearance of resonances and resonance elliptical rings (Buta 2017).

The positions of the resonances in a galactic disc are determined from the condition:

$$\frac{m}{n} = \frac{\kappa}{\Omega - \Omega_b}, \quad (1)$$

where  $m$  is the number of full epicyclic oscillations that a star makes during  $n$  revolutions relative to the bar. Usually the case  $n = 1$  is considered. The ratio  $m/n = +2/1$  determines the position of the Inner Lindblad Resonance (ILR), and the ratio  $m/n = -2/1$  determines the radius

of the Outer Lindblad resonance (OLR). The resonances  $m/n = \pm 4/1$  are also of great interest (Contopoulos 1983; Contopoulos & Grosbol 1989; Athanassoula 1992a).

Resonance elliptical rings in barred galaxies arise due to adjustment of epicyclic motions of stars in accordance with their orbital rotation with respect to the bar. There are three basic types of rings: nuclear ( $n$ ), inner ( $r$ ), and outer ( $R_1$ , and  $R_2$ ) rings. Nuclear rings are usually located near the ILR of the bar and are elongated perpendicular to the bar, inner rings lie near the Corotation Radius (CR) and are usually elongated parallel to the bar, outer rings are located near the OLR and have two possible orientations: the rings  $R_1$  and pseudo-rings (broken rings)  $R'_1$  are aligned perpendicular to the bar, but the rings  $R_2$  and pseudo-rings  $R'_2$  are elongated parallel to the bar. From the two types of outer rings, ring  $R_1$  is located a bit closer to the Galactic center than ring  $R_2$  (Schwarz 1981; Buta 1995; Buta & Combes 1996; Buta & Crocker 1991; Byrd et al. 1994; Rautiainen & Salo 1999, 2000; Rodriguez-Fernandez & Combes 2008; Sormani et al. 2018). Rautiainen & Salo (2000) also found cyclic or semi-cyclic

\* E-mail: anna@sai.msu.ru

variations in the morphology of the outer rings: from  $R_2$  to  $R_1R_2$  and back. The fraction of systems with outer rings among galaxies with a moderate or a strong bar is as high as 20–30 per cent (Comeron et al. 2014).

In addition to the resonance elliptical rings, there are also lenticular structures that are very similar to the rings but have flatter density distributions, especially at the outer boundary. These can have the form of inner ( $l$ ) and outer lenses ( $L$ ) whose orientations in most cases coincide with the orientations of the inner ( $r$ ) and outer ( $R_1$ ) rings, respectively (Kormendy 1979; Athanassoula et al. 1982; Buta & Combes 1996; Laurikainen et al. 2011).

The backbone of resonance rings are direct stable periodic orbits which are followed by a large number of stars in quasi-periodic orbits. Inside the CR family of periodic orbits  $x_1$  is elongated along the bar and form its backbone. Near the OLR, the main family of periodic orbits  $x_1$  splits into two families:  $x_1(1)$  and  $x_1(2)$ . The periodic orbits  $x_1(2)$  are elongated perpendicular to the bar and lie between the resonances  $-4/1$  and OLR while the periodic orbits  $x_1(1)$  are elongated parallel to the bar and are located outside the OLR. In the case of a weak bar, the stable periodic orbits  $x_1(2)$  and  $x_1(1)$  support the rings  $R_1$  and  $R_2$ , respectively (Contopoulos & Papayannopoulos 1980; Contopoulos & Grosbol 1989; Schwarz 1981; Buta & Combes 1996).

In the case of a strong bar, the periodic orbits  $x_1(2)$  lying between the resonances  $-4/1$  and OLR become unstable (Contopoulos & Papayannopoulos 1980; Contopoulos & Grosbol 1989). However, even in this case, spiral arms and ring-like structures can be supported for some time by sticky-chaotic orbits (Contopoulos & Harsoula 2010) associated with the unstable equilibrium points  $L_1$  and  $L_2$  located at the ends of the bar (Athanassoula et al. 2009a,b, 2010).

In barred galaxies, there are Lagrange equilibrium points at which the bar gravity is balanced by the centrifugal inertial force. The Lagrange equilibrium points  $L_1$ ,  $L_2$ ,  $L_4$  and  $L_5$  are located near the CR on the minor ( $L_4$  and  $L_5$ ) and major ( $L_1$  and  $L_2$ ) axes of the bar. In the neighborhood of the stable equilibrium points  $L_4$  and  $L_5$ , there are two types of periodic orbits: short-period (SPO) and long-period (LPO) orbits. Short-period orbits are similar to a small ellipse and their orbital period is close to the epicyclic one while long-period orbits resemble a banana and their orbital period is several times longer. Most non-periodic banana-type orbits are a combination of short- and long-period oscillations (Contopoulos 1978, 1983; Contopoulos & Grosbol 1989; Binney & Tremaine 2008).

A concentration of stars near the equilibrium points  $L_4$  and  $L_5$  can also support spiral arms (Barbanis 1970) and ring-like structures, provided the stars have the appropriate energy and are not trapped around them (Danby 1965; Patsis & Tsigaridi 2017).

The periodic enhancement of either trailing or leading segments of the resonance elliptical structures can be found in many studies. We can clearly see the periodic motion of the density maxima along spiral arms emanating from the bar ends in the study by Contopoulos (2009, Fig. 14 therein). Furthermore, the stellar response of the model with the Ferrers bar in Athanassoula (1992b) demonstrates the predominance of leading or trailing spiral arms at different

time instants. On the other hand, the gas response always shows the formation of the overdensity on the leading side of the bar.

The notion of resonance as a certain radius is true only for circular orbits, but for elliptical orbits, we deal with a Lindblad Zone (Struck 2015a,b).

Stellar motions near the bar resonances are often described in terms of angle-action variables (Weinberg 1994). It is often convenient to consider the frequency of the resonance:

$$\Omega_s = n\Omega_R + m(\Omega - \Omega_b), \quad (2)$$

where  $\Omega_R$  is the frequency of radial oscillations. In the epicyclic approximation  $\Omega_R$  coincides with the epicyclic frequency,  $\Omega_R = \kappa$ . The value  $n = 0$  corresponds to the Corotation Resonance, but the combination of  $n = \pm 1$  and  $m = 2$  describes the Lindblad resonances. The integral of  $\Omega_s$  over the time determines the so-called slow angle variable

$$\theta_s = \int_0^t \Omega_s(t') dt', \quad (3)$$

which varies very slowly near the resonances. The slow angle corresponds to the precession angle of the orbit relative to the bar, whereas the fast angle variable,  $\theta_f$ , describes the motion of the star around its orbit. Weinberg (1994) showed that the slow angle  $\theta_s$  can change in two ways: the direction of orbit elongation may oscillate within certain angles or may rotate without any restriction on angles. The study of orbits near the resonances of the bar became especially salient in the last decade (Struck 2015b; Monari et al. 2017; Trick et al. 2021; Chiba, Friske & Schönrich 2021; Chiba & Schönrich 2021, 2022).

The studies carried out by our team provided extensive evidence for the presence of the Galactic outer resonance rings located near the solar circle. We developed models of the Galaxy with the outer resonance rings  $R_1$  and  $R_2$  which reproduce well the kinematics of young objects (OB-associations, young clusters, classical Cepheids) in the 3-kpc solar neighborhood (Melnik & Rautiainen 2009; Rautiainen & Melnik 2010; Melnik et al. 2015, 2016). The velocity dispersion of these objects in the Galactic plane is  $\sim 10 \text{ km s}^{-1}$ . Our models can also explain the distribution of star-forming regions in the Galactic disc (Melnik & Rautiainen 2011). The best agreement between model and observed velocities of OB associations corresponds to the model with the bar angular velocity of  $\Omega_b = 50 \pm 2 \text{ km s}^{-1} \text{ kpc}^{-1}$  (Melnik 2019).

In our latest study (Melnik et al. 2021), we compared the model and observed velocity distributions of old disc stars along the Galactocentric distance  $R$ . The radial velocity dispersion of these stars at the solar Galactocentric distance is  $\sim 30 \text{ km s}^{-1}$ . The best agreement between the model and observed velocities is achieved for the model with the bar angular velocity of  $\Omega_b = 55 \pm 3 \text{ km s}^{-1} \text{ kpc}^{-1}$ , the position angle of the bar with respect to the Sun of  $\theta_b = 45 \pm 15^\circ$  and the age of the Galactic bar of  $1.8 \pm 0.5 \text{ Gyr}$ .

Any elliptical ring can be divided into 4 similar segments each of which can be represented as a fragment of a trailing ( $R$  decreases with increasing  $\theta$ ) or a leading ( $R$  increases with increasing  $\theta$ ) spiral, where the galactocentric angle  $\theta$  increases in the sense of the galactic rotation.

In this paper, we study periodic changes in the morphology of resonance rings using the Galactic model from Melnik et al. (2021). We have found the periodic enhancement of either trailing or leading segments in the region of the inner combined ring and in the region of the outer rings which have different periods and are likely to appear due to different causes.

In Section 2 we compare the distributions of observed velocities along the distance  $R$  derived from the *Gaia* DR3 and *Gaia* EDR3 data. Section 3 describes the dynamical model of the Galaxy. In section 4 we analyze periodic changes in the stellar density in the region of the inner ring and the outer rings. In Section 5 we study orbits that can support the inner combined ring and propose a mechanism producing the periodic changes in the morphology of the inner ring. In Section 6 we study the orbits near the OLR of the bar and show that the librations of the direction of orbit elongation can produce changes in the morphology of the outer rings. The discussion and main conclusions are given in Section 7.

## 2 OBSERVATIONS

In our latest study (Melnik et al. 2021), we selected stars from the *Gaia* EDR3 catalogue (Gaia Collaboration, Prusti, de Bruijne et al. 2016; Gaia Collaboration, Brown, Vallenari et al. 2021; Lindegren, Klioner, Hernandez et al. 2021) that lie near the plane of the Galaxy  $|z| < 200$  pc and in the sector of the Galactocentric angles  $|\theta - \theta_0| < 15^\circ$ , where  $\theta_0$  is the azimuthal angle of the Sun with respect to the bar major axis ( $\theta_0 = -\theta_b$ ), and calculated the median radial,  $V_R$ , azimuthal,  $V_T$ , and vertical,  $V_Z$ , velocity components in  $\Delta R = 250$ -pc wide bins along the distance  $R$ . The final sample included  $2.39 \times 10^6$  *Gaia* EDR3 stars. Our model appeared to reproduce well the observed dependences of the velocities  $V_R$  and  $V_T$  on  $R$  in the distance range  $|R - R_0| < 1.5$  kpc, where  $R_0$  is the Galactocentric distance of the Sun.

We adopt the solar Galactocentric distance  $R_0 = 7.5$  kpc (Glushkova et al. 1998; Nikiforov 2004; Eisenhauer et al. 2005; Nishiyama et al. 2006; Feast et al. 2008; Groenewegen, Udalski & Bono 2008; Reid et al. 2009; Dambis et al. 2013; Francis & Anderson 2014; Boehle et al. 2016; Branham 2017; Iwanek et al. 2023). Generally, the choice of the value of  $R_0$  within the limits 7–9 kpc has practically no effect on the results.

In this study we calculate the dependences of  $V_R$ ,  $V_T$ , and  $V_Z$  on  $R$  for *Gaia* DR3 data (Gaia Collaboration, Vallenari, Brown et al. 2022). The final sample includes  $8.32 \times 10^6$  *Gaia* DR3 stars. Fig. 1 shows the distributions of the velocities  $V_R$ ,  $V_T$ , and  $V_Z$  and those of the velocity dispersions  $\sigma_R$ ,  $\sigma_T$ , and  $\sigma_Z$  derived from *Gaia* DR3 and *Gaia* EDR3 data. Average differences between the velocities derived from *Gaia* EDR3 and *Gaia* DR3 data do not exceed  $1 \text{ km s}^{-1}$ . The main difference is observed in the  $V_R$ -velocity profile (Fig. 1a), which has a minimum at  $R = 8.5$  kpc with a depth of  $-5.2$  and  $-2.8 \text{ km s}^{-1}$  according to *Gaia* DR3 and *Gaia* EDR3 data, respectively. However, this difference does not change the

general tendency: the smooth fall of radial velocities near the solar circle.

The radial profile of the velocity dispersion  $\sigma_R$  derived from *Gaia* DR3 data in the distance interval  $R = 5$ –11 kpc can be approximated by the exponential law with the scale length of  $S_R = 23.7 \pm 1.6$  kpc, which agrees with the estimate  $S_R = 22.3 \pm 1.4$  kpc derived from *Gaia* EDR3 data.

Note an important feature, which has received little attention, namely – a sharp drop in the azimuthal velocity  $V_T$  at  $R \approx 4.0$ –5.5 kpc (Fig. 1c). This effect is likely due to the lack of stars associated with the thin disc compared to the fraction of stars associated with the thick disc and halo in this region. Extinction in Galactic midplane increases very rapidly towards the Galactic center (Neckel & Klare 1980; Marshall et al. 2006; Melnik et al. 2015, 2016). The sources with line-of-sight velocity listed in the *Gaia* DR3 (*Gaia* EDR3) catalogue are mostly brighter than  $G = 14^m$  ( $G = 13^m$ ) (Gaia Collaboration, Vallenari, Brown et al. 2022; Gaia Collaboration, Brown, Vallenari et al. 2018; Sartoretti et al. 2018; Gaia Collaboration, Katz, Antoja et al. 2018; Katz et al. 2019). As extinction increases, stars associated with the thick disc and halo are more likely to have line-of-sight velocity measurements compared to thin-disc stars. There are two reasons for this: the distribution along  $z$  and colour. Thin-disc stars strongly concentrate to the Galactic midplane, where extinction is stronger compared to thick-disc and halo stars, and therefore the fraction of thick-disc and halo stars in the  $|z| < 200$ -pc layer that are brighter than  $G = 14^m$  must increase with increasing extinction. In addition, extinction has stronger effect on blue stars than on red ones, and therefore the fraction of red stars brighter than  $G = 14^m$  must increase with increasing extinction. Thus, the sharp drop in the velocity  $V_T$  towards the Galactic center seems to be caused by selection effects.

Our models reproduce well the drop in the velocity  $V_T$  at Galactocentric distances  $R = 7.5$ –10 kpc. This region lies in the direction towards the Galactic anticenter, where extinction is small. Here the decrease in the azimuthal velocity  $V_T$  is caused by the influence of the bar.

Note that the median velocities  $V_Z$  in the direction perpendicular to the Galactic plane derived from the *Gaia* DR3 data do not exceed  $|V_Z| < 3 \text{ km s}^{-1}$  in the distance interval  $R = 4$ –11 kpc and do not exceed  $|V_Z| < 1 \text{ km s}^{-1}$  in the distance interval  $|R - R_0| < 1.5$ . Quite strong variations of both  $V_R$  and  $V_T$  over the Galactocentric distance interval  $R = 6$ –10 kpc combined with the absence of noticeable systematic motions in  $Z$ -direction suggest that stellar motions in the Galactic plane and in the vertical direction are independent. This justifies our use of a 2D-model of the Galaxy.

## 3 MODEL

We used a 2D-model of the Galaxy with analytical potential and studied the response of the stellar disc to the bar perturbation. Our model includes the bulge, bar, exponential disc, and halo. We used the analytical Ferrers ellipsoid to calculate the potential of the bar (de Vaucouleurs & Freeman 1972; Pfenniger 1984; Binney & Tremaine 2008; Sellwood & Wilkinson 1993). The major and minor axes of the bar are  $a = 3.5$  and  $b = 1.35$

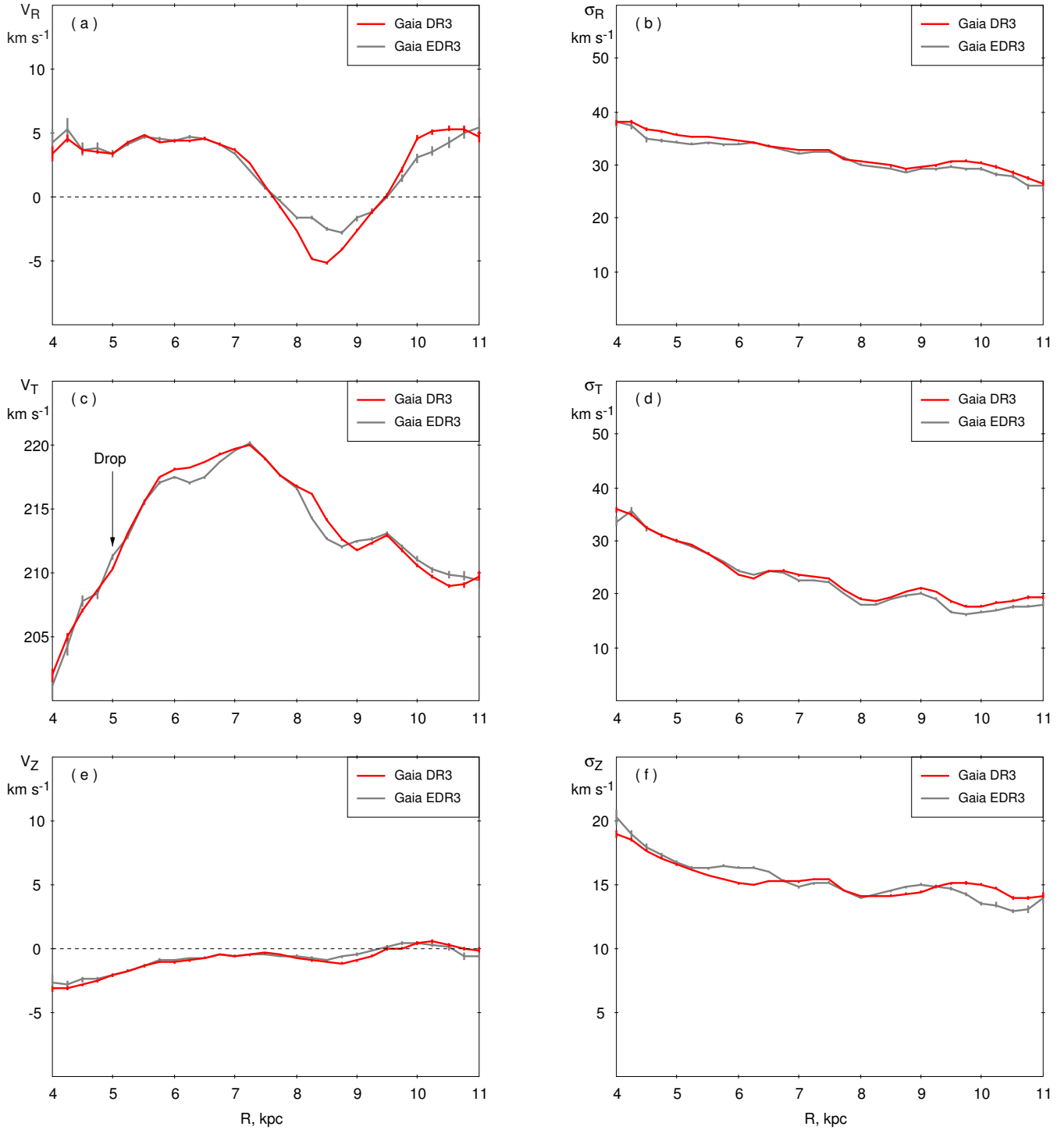


**Figure 1.** (Left panel) Dependences of the radial  $V_R$  (a), azimuthal  $V_T$  (c), and vertical  $V_Z$  (e) components of the median velocity on Galactocentric distance  $R$  derived from *Gaia* DR3 (red lines) and *Gaia* EDR3 data (gray lines) in  $\Delta R = 250$ -pc wide bins. The vertical lines on the curves indicate random errors in the determination of the median velocities. The arrow on frame (c) indicates the drop in the median velocity  $V_T$  which seems to be due to selection effects. (Right panel) Dependences of the median dispersion of the radial  $\sigma_R$  (b), azimuthal  $\sigma_T$  (d) and vertical  $\sigma_z$  (f) velocities on Galactocentric distance  $R$ . The distributions of the velocities  $V_R$ ,  $V_T$ ,  $V_Z$  and the velocity dispersions  $\sigma_R$ ,  $\sigma_T$ , and  $\sigma_Z$  derived from *Gaia* DR3 and *Gaia* EDR3 data can be seen to generally agree well with each other.

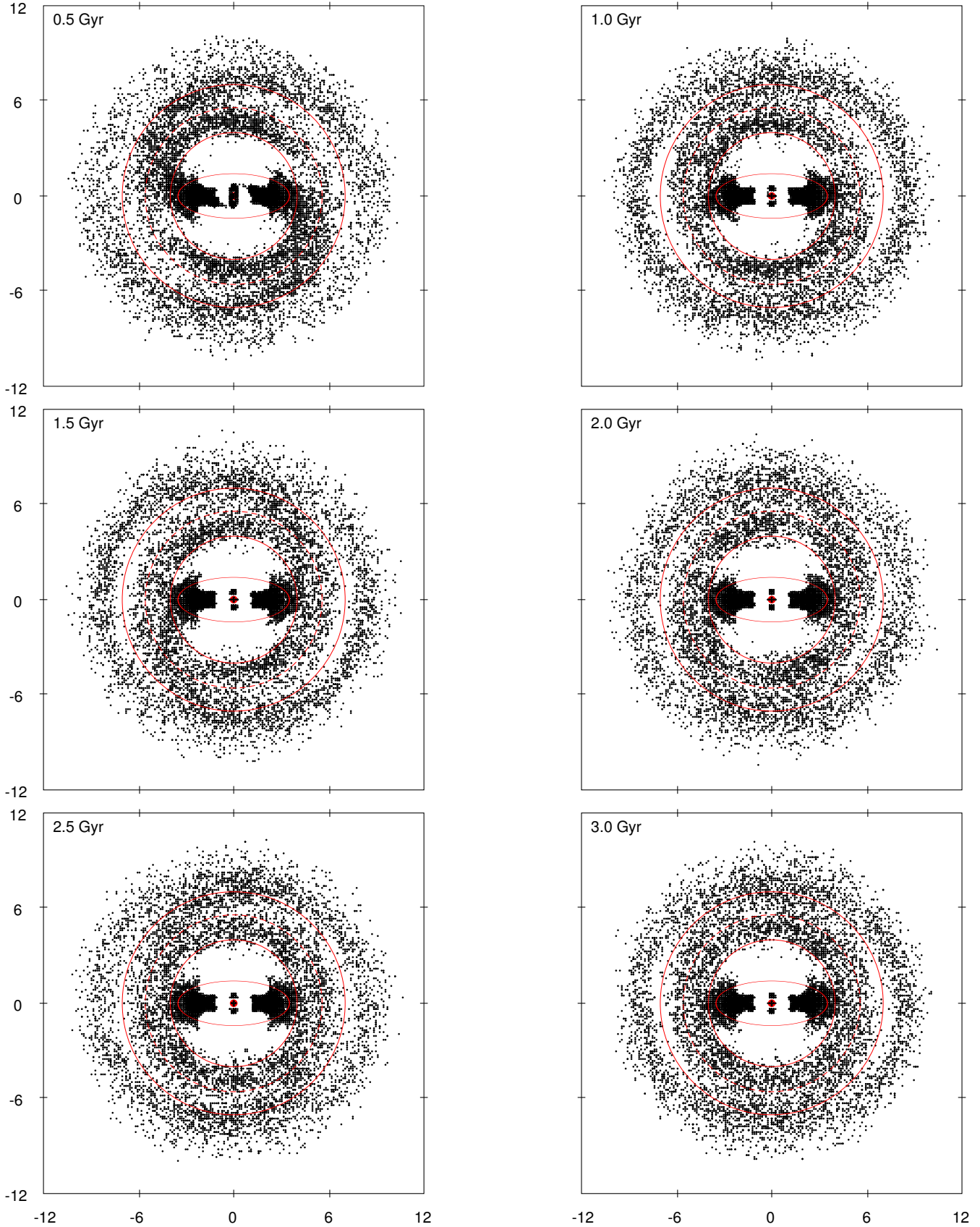


**Figure 2.** Distributions of stars in the Galactic plane at the time instants 0.5, 1.0, 1.5, 2.0, 2.5, and 3.0 Gyr processed by the program that increases contrast. The parameter  $h$ , which controls the contrast, is  $h = 1.5$ . In these plots 10 per cent of stars are shown. The ellipse shows the position of the bar. The red solid lines indicate the positions of the CR and OLR, and the dashed line shows the position of the resonance  $-4/1$ . The Galaxy rotates counterclockwise. The size of each frame is  $24 \times 24 \text{ kpc}^2$ .

kpc, respectively. The mass of the bar is  $1.2 \times 10^{10} M_{\odot}$ . The angular velocity of the bar rotation is  $\Omega_b = 55 \text{ km s}^{-1} \text{ kpc}^{-1}$  which corresponds to the best agreement between the model and observed distributions of the velocities  $V_R$  and  $V_T$  in Galactocentric distance  $R$ . The CR of the bar is located at  $R_{RC} = 4.04 \text{ kpc}$ , the resonance  $-4/1$  and the OLR of the bar lie at  $R_{-4/1} = 5.52$  and  $R_{OLR} = 7.00 \text{ kpc}$ , respectively. The bar grows slowly, approaching full strength by  $T_b \sim 0.45 \text{ Gyr}$ , which is equal to four bar rotation periods, but the  $m = 0$  component of the bar is included in the model from the very beginning. It means that the model is initially axisymmetric, but then its non-axisymmetric perturbation, i.e. the bar component, slowly increases. The mass of the bar is conserved during the simulation. The strength of the bar after it reaches a full power is  $Q_b = 0.3142$ , which corresponds to strong bars (Block et al. 2001; Buta, Laurikainen & Salo 2004; Díaz-García et al. 2016).

The model of the Galaxy includes the exponential disc with the mass of  $M_d = 3.25 \times 10^{10} M_{\odot}$  and the characteristic scale of  $R_d = 2.5 \text{ kpc}$ . The total mass of the model disc and the bar is  $4.45 \times 10^{10} M_{\odot}$ , which agrees with other estimates of the mass of the Galactic disc lying in range  $3.5\text{--}5.0 \times 10^{10} M_{\odot}$  (Shen et al. 2010; Fujii et al. 2019).

The average azimuthal velocities  $\overline{V_T}$  in the velocity distribution of stars at  $t = 0$  are determined by solving the Jeans equation. We set the radial scale length of the initial distribution of radial velocity dispersion equal to 20 kpc.

The classical bulge is represented by a Plummer sphere with a mass of  $M_{bg} = 5 \times 10^9 M_{\odot}$  (Nataf 2017; Fujii et al. 2019). The halo is modeled as an isothermal sphere (Binney & Tremaine 2008).

Model particles represent the motions of stars of the thin disc. The initial radial-velocity dispersion of model particles at the solar distance is  $\sigma_R = 30.5 \text{ km s}^{-1}$ , which is close to the observed value,  $\sigma_R = 32.0 \text{ km s}^{-1}$  (*Gaia* DR3).

Note that our model has an order of symmetry equal to  $m = 2$ , i.e. each star with coordinates  $(x, y)$  and velocities  $(V_x, V_y)$  has a twin with coordinates  $(-x, -y)$  and velocities  $(-V_x, -V_y)$ . For a more detailed description of the model, see Melnik et al. (2021).

## 4 PERIODIC CHANGES IN THE RING MORPHOLOGY

### 4.1 Density distribution in the Galactic disc

The model stellar disc forms the outer resonance rings by the time  $\sim 1 \text{ Gyr}$ . However, the perturbations of the stellar density in the disc are small which is a consequence of the large velocity dispersion. To see the density perturbations we should increase the density contrast in the disc.

Fig. 2 shows the distributions of stars in the Galactic plane at the time instants 0.5, 1.0, 1.5, 2.0, 2.5, and 3.0 Gyr processed by a program that increases the contrast. The parameter  $h$  controls the contrast: the higher  $h$ , the higher the contrast. The essence of processing procedure is that for each star we calculate the average density  $\Sigma_1$  of other stars located within a radius of 50 pc from the star considered and compare  $\Sigma_1$  with the initial density  $\Sigma_0$  at  $t = 0$ , when the distribution of stars is purely exponential. If  $\Sigma_1/\Sigma_0 \leq 1.0$  then the star is not included in the image. If  $\Sigma_1/\Sigma_0 \geq h$ , then

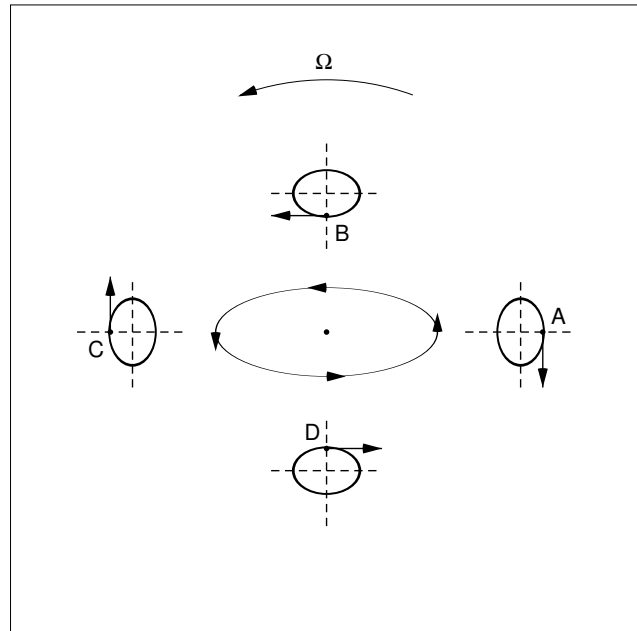


**Figure 3.** Motion of a star in an elliptical orbit supporting the bar. The star is located inside the CR and its motion is considered in the reference frame of the rotating bar. On the major axis of the bar, the star is at the outermost points of the epicycle (*A* and *C*) and the positive velocity of orbital rotation (i.e. motion in the sense of Galactic rotation) adds up with the negative velocity of the epicyclic motion, and vice versa, on the minor axis of the bar, the star is at the points of the epicycle closest to the center (*B* and *D*) and the positive velocity of the orbital rotation adds up with the positive velocity of the epicyclic motion. This means that the star moves at a smaller velocity on the major axis of the bar than on the minor one. Consequently, the density of stars on the major axis of the bar must be higher than on the minor one.

the star is included in the image with the probability  $P = 100$  per cent. If the density ratio has intermediate values,  $1.0 < \Sigma_1/\Sigma_0 < h$ , then the star is included in the image with the probability:

$$P = \frac{\Sigma_1 - \Sigma_0}{\Sigma_0(h - 1)} 100\%, \quad (4)$$

which increases linearly from 0 to 100 per cent with increasing the ratio  $\Sigma_1/\Sigma_0$  from 1.0 to  $h$ . The contrast parameter in Fig. 2 is  $h = 1.5$ .

Fig. 2 shows the presence of an inner pseudo-ring located between the CR and the resonance  $-4/1$ , the outer resonance ring  $R_2$  located outside the OLR ( $R > R_{OLR}$ ), as well as the appearance of either trailing ( $t = 0.5, 1.0, 2.5, 3.0 \text{ Gyr}$ ) or leading ( $t = 1.5, 2.0 \text{ Gyr}$ ) spiral arms located in the region between the resonance  $-4/1$  and the OLR which are the trailing and leading segments of the ring  $R_1$ , respectively. Near the OLR of the bar the outer ring  $R_1$  smoothly transits into the ring  $R_2$ .

Fig. 2 shows that inside the bar (red ellipse) the stellar density increases only near the ends of the bar which may come as a surprise. Though epicyclic approximation is not valid in the bar region for quantitative estimates, it can help understand this fact at a qualitative level. Fig. 3 schematically illustrates the motion of a star in an elliptical orbit supporting the bar. We can see that stars move with

a smaller velocity on the major axis of the bar than on the minor one. Consequently, the density of stars on the major axis of the bar must be higher than on the minor one. This relation is a consequence of the motion of stars in closed orbits and the formation of elliptical orbits from circular ones uniformly populated by stars.

Fig. 2 also shows that the central region of the Galaxy is relatively empty. This fact is due to a fast fall of stars onto the Galactic center during the bar formation. By the time  $t = 0.5$  Gyr, 19 per cent of stars initially located within the distance interval  $0.02 < R < 1$  kpc are found to be inside a tiny region of  $R < 0.02$  kpc and the integration of their orbits is stopped. The rapid loss of the angular momentum is possibly due to the growth of the bar rotating at a constant angular velocity, which is considerably smaller than the initial angular velocities of most of stars in the central region.

In general, we had a choice: either to compare the local value (local in place and in time) of the stellar density with the initial density distribution or with the current averaged value of the density at the radius considered. The first approach is more suitable to search for ring structures and the second one – for identification of open (with a large pitch angle) spiral arms (for example, Melnik & Rautiainen 2013).

An elementary logarithmic spiral wave is defined by the equation:

$$R = C e^{\tan(\gamma)(\theta - \theta_1)}, \quad (5)$$

where  $\gamma$  is the pitch angle of spiral arms,  $R$  and  $C$  are the Galactocentric distances to the spiral arm at the Galactocentric angles  $\theta$  and  $\theta_1$ , respectively. If  $\theta$  increases in the sense of Galactic rotation then the negative and positive values of  $\gamma$  describe the trailing and leading spiral arms, respectively. Note that if we subdivide an elliptical ring into four parts along its two axes of symmetry, then each quarter of the ring can be approximated by a fragment of a leading or a trailing spiral arm. Thus an elliptical ring can be represented by the superposition of trailing and leading spiral perturbations with the same absolute values of the pitch angle  $|\gamma|$ .

The amplitudes of the spiral oscillations in the distribution of  $N$  objects in the galactic plane can be determined from the formula:

$$A(p, m) = \frac{1}{N} \sum_{j=1}^N e^{-i(m\theta_j + p \ln R_j)}, \quad (6)$$

where  $p = -m/\tan\gamma$  and  $m$  is the number of spiral arms (Kalnajs 1971; Considere & Athanassoula 1982; Binney & Tremaine 2008). As elliptical rings have an order of symmetry equal to  $m = 2$ , hereafter we consider only  $m = 2$  amplitudes. The parameter  $p$  determines the pitch angle  $\gamma$  of spiral arms:  $p > 0$  and  $p < 0$  correspond to trailing and leading spiral arms, respectively.

Fig. 4 (a, c) shows the distributions of stars in the plane  $(\theta, \ln R/R_{CR})$  computed for the time instants  $t = 1.0$  and  $t = 1.5$  Gyr. It is evident from the figure that stars concentrate to the straight lines which correspond to the positions of the logarithmic spiral arms. The slope of the lines to the left ( $t = 1.0$  Gyr) or to the right ( $t = 1.5$  Gyr) indicates the

predominance of trailing ( $t = 1.0$  Gyr) or leading ( $t = 1.5$  Gyr) spiral arms.

Fig. 4 (b, d) shows the amplitudes  $|A_2|$  of the Fourier transforms calculated in three regions:  $R_{CR} < R < R_{-4/1}$  (inner ring),  $R_{-4/1} < R < R_{OLR}$  (outer ring  $R_1$ ), and  $R_{OLR} < R < R_{OLR} + 1.5$  kpc (outer ring  $R_2$ ). We can see that at the time moment  $t = 1.0$  Gyr maximum values of the amplitude  $|A_2|$  correspond to  $p \approx 10$  in all three regions, which indicates the predominance of trailing spiral arms with the pitch angle of  $\gamma \approx -10^\circ$ . At the time  $t = 1.5$  Gyr, trailing spiral arms dominate only in the region of the inner ring,  $R_{CR} < R < R_{-4/1}$ , while leading spirals dominate in two other regions.

Note that we show the distribution of stars in the plane  $(\theta, \ln R/R_{CR})$  (Fig. 4 a, c) only for stars that remain in the sample after processing the sample by the contrast increasing program (Eq. 4), but compute the Fourier amplitudes  $|A_2|$  with the use of all stars located in the region considered.

Fig. 5 (a, c) shows the distributions of stars in the plane  $(\theta, \ln R/R_{CR})$  at  $t = 2.0$  and  $t = 2.5$  Gyr. As is evident from the figure, stars in the region of the outer rings concentrate to the straight lines inclined to the right ( $t = 2.0$  Gyr) and to the left ( $t = 2.5$  Gyr) which indicates the predominance of leading ( $t = 2.0$  Gyr) and trailing ( $t = 2.5$  Gyr) spiral arms, respectively.

Fig. 5 (b, d) shows that in the region of the outer rings maximum values of the amplitudes  $|A_2|$  correspond to negative ( $t = 2.0$  Gyr) or positive ( $t = 2.5$  Gyr) values of  $p$ , respectively, which indicates the predominance of leading ( $t = 2.0$  Gyr) or trailing ( $t = 2.5$  Gyr) spiral arms. In the region of the inner ring,  $R_{CR} < R < R_{-4/1}$ , we see the predominance of trailing spirals at the time  $t = 2.0$  Gyr and the symmetry in the distribution of the amplitude  $|A_2|$  with respect to the vertical line  $p = 0$  at the time  $T = 2.5$  Gyr, which is typical for elliptical structures. A comparison of Fig. 4 and Fig. 5 reveals the changes in maximum values of the amplitudes  $|A_2|$  in each region.

Thus, we have found changes in the morphology of the inner ring and outer rings, namely the enhancement (density increase) of either trailing or leading segments of the elliptical rings.

To prove that the changes in morphology discussed here are not due to random fluctuations in density and velocity, we build model 2, which differs from model 1 (considered here) by random deviations in the density and velocity distributions at  $t = 0$ . The random changes are hardly seen in the distribution of stars in the Galactic plane, but they are visible in variations of the Fourier amplitudes (Fig. 6) and we discuss them in section 4.2.

## 4.2 Periodic changes in the density of trailing and leading segments of the resonance rings

Let us consider periodic changes in the morphology of the resonance rings and determine the periods of these variations. Fig. 6 (left panel) shows the variations in maximum values,  $A_{max}$ , of the Fourier amplitude  $|A_2|$  calculated in the region of the inner ring and in the region of the outer rings as a function of time  $t$ . Fig. 6 (right panel) shows variations in the parameter  $p_{max}$  corresponding to maximum value of the amplitude  $|A_2|$ . The parameter  $p_{max} = -m/\tan\gamma$  char-

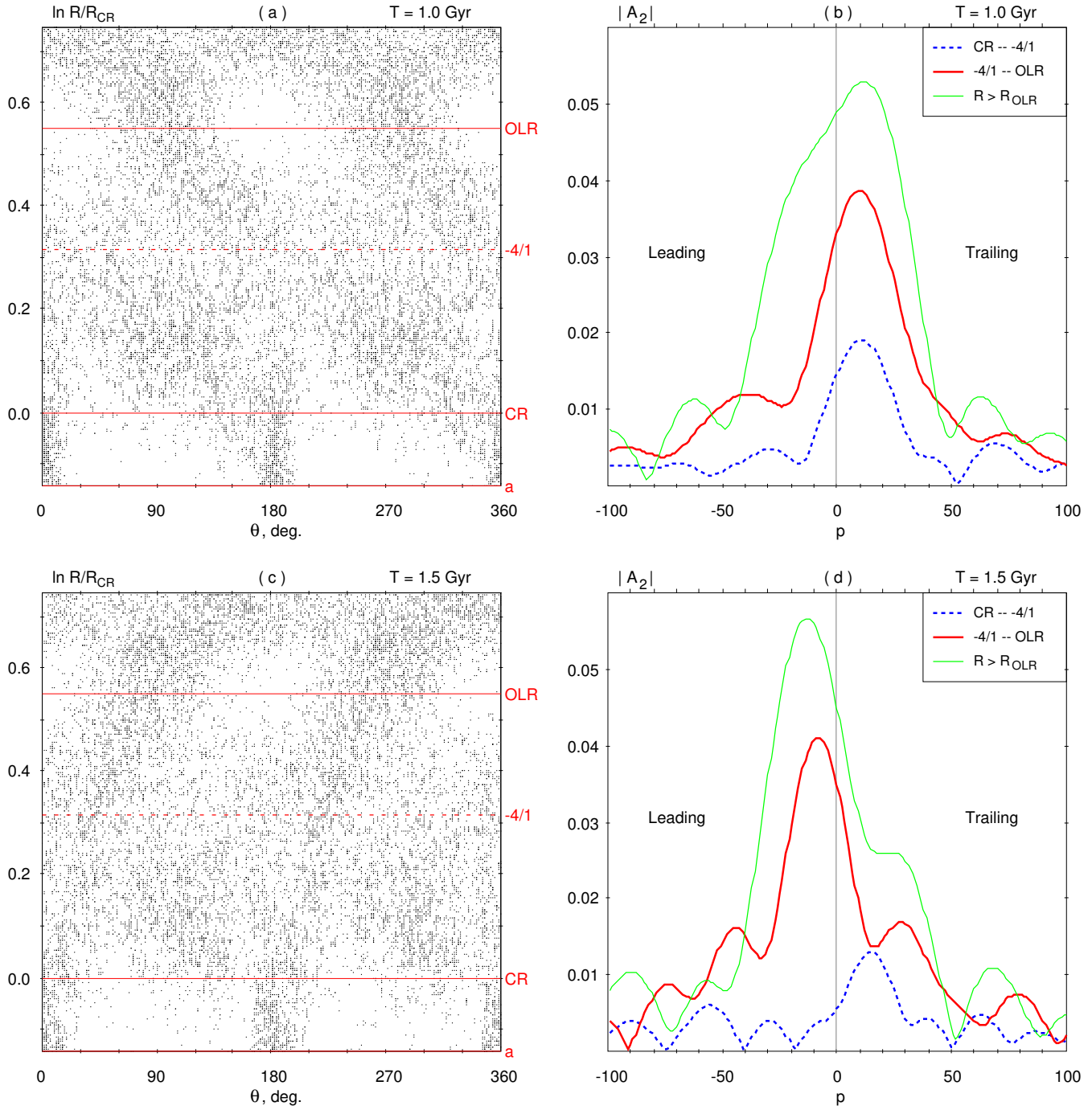


**Figure 4.** Positions of the spiral arms and the Fourier amplitudes  $|A_2|$  calculated for the time instants  $t = 1.0$  Gyr (the upper row) and  $t = 1.5$  Gyr (the bottom row). (a, c) Distributions of stars in the  $(\theta, \ln R/R_{CR})$  plane. The red horizontal lines indicate the positions of the resonances and the bar major axis  $a$ . We can see that stars concentrate to the straight lines that correspond to the positions of the logarithmic spiral arms. The slope of the lines to the left ( $t = 1.0$  Gyr) or to the right ( $t = 1.5$  Gyr) indicates the predominance of trailing ( $t = 1.0$  Gyr) or leading ( $t = 1.5$  Gyr) spiral arms, respectively. (b, d) The Fourier amplitudes  $|A_2|$  of the expansions of the distributions of stars into spiral harmonics calculated in three regions:  $R_{CR} < R < R_{-4/1}$  (inner ring),  $R_{-4/1} < R < R_{OLR}$  (outer ring  $R_1$ ) and  $R_{OLR} < R < R_{OLR} + 1.5$  kpc (outer ring  $R_2$ ). The parameter  $p$  determines the pitch angle  $\gamma$  of spiral arms,  $p = -m/\tan \gamma$ , where  $p > 0$  and  $p < 0$  correspond to trailing and leading spiral arms, respectively. The vertical line corresponds to  $p = 0$ . We can see that at the time  $t = 1.0$  Gyr maximum values of the amplitudes  $|A_2|$  indicate the predominance of trailing spiral arms in all three regions, but at  $t = 1.5$  Gyr trailing arms dominate only in the region of the inner ring,  $R_{CR} < R < R_{-4/1}$ , whereas leading spirals prevail in the other two regions.



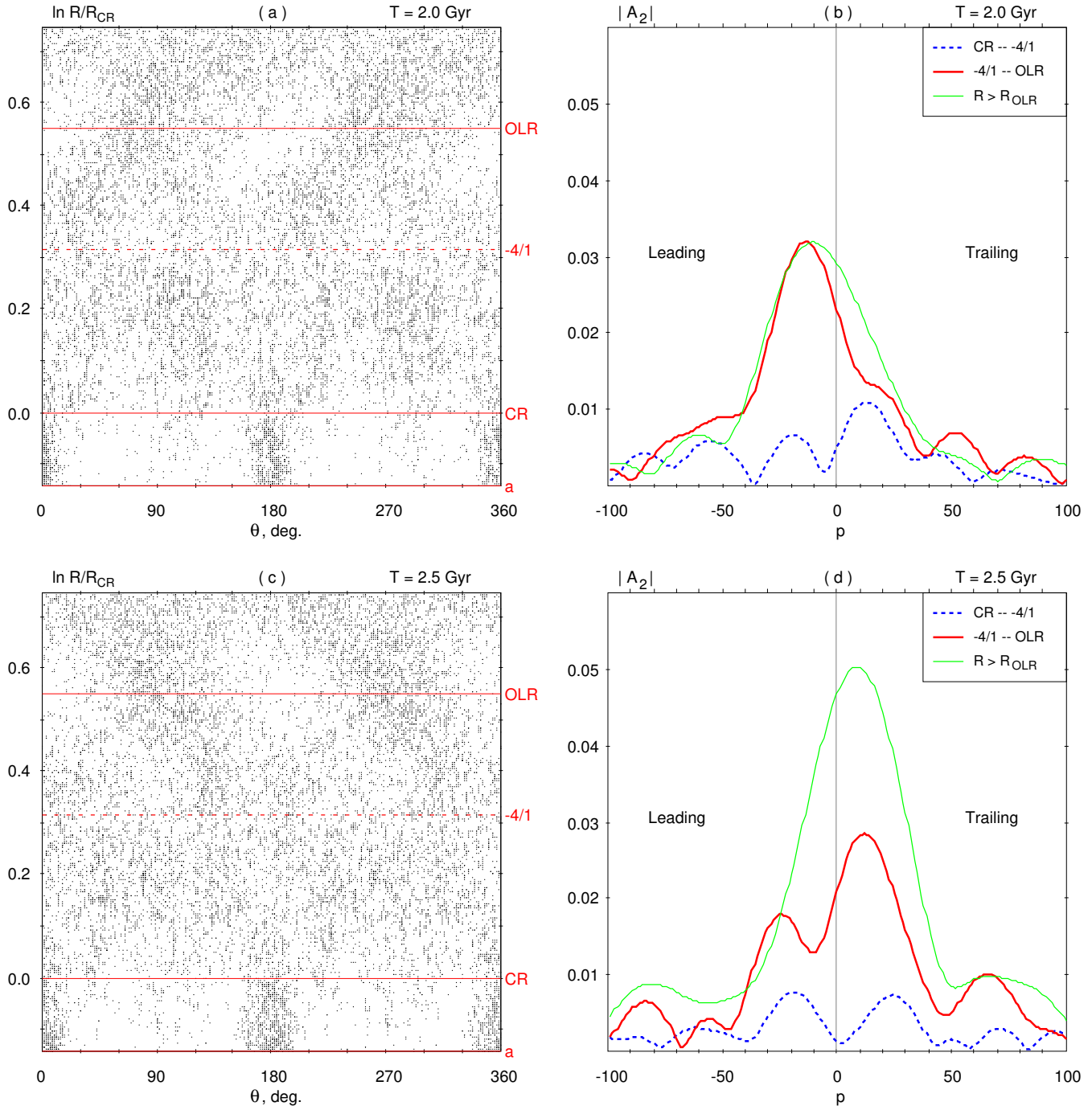


**Figure 5.** Positions of the spiral arms and the Fourier amplitudes  $|A_2|$  calculated for the time instants  $t = 2.0$  Gyr (the upper row) and  $t = 2.5$  Gyr (the bottom row). (a, c) It can be seen that in the region of the outer rings,  $R_{-4/1} < R < R_{OLR} + 1.5$  kpc, stars concentrate to the straight lines inclined to the right ( $t = 2.0$  Gyr) or to the left ( $t = 2.5$  Gyr), which indicates the predominance of leading ( $t = 2.0$  Gyr) or trailing ( $t = 2.5$  Gyr) spirals, respectively. (b, d) In the region of the outer rings, maximum values of the amplitude  $|A_2|$  correspond to negative ( $t = 2.0$  Gyr) or positive ( $t = 2.5$  Gyr) value of  $p$ , which indicates the predominance of leading ( $t = 2.0$  Gyr) or trailing ( $t = 2.5$  Gyr) spiral arms, respectively. In the region of the inner ring,  $R_{CR} < R < R_{-4/1}$ , we can see the predominance of trailing spirals at  $t = 2.0$  Gyr and the symmetry in the amplitude  $|A_2|$  with respect to the vertical line  $p = 0$  at the time  $t = 2.5$  Gyr which is typical for elliptical structures. For more details, see caption to Fig. 4.

acterizes the pitch angle  $\gamma$  of a two-armed spiral pattern, which predominates at the time considered. We can see that the parameters calculated for models 1 and 2 that differ from one another by random deviations of their initial conditions agree within the random fluctuations. The period of varia-

tions of the amplitude  $A_{max}$  in the region of the inner ring ( $R_{CR} < R < R_{-4/1}$ ) is significantly shorter than that in the region of the outer rings  $R_1$  and  $R_2$  ( $R_{-4/1} < R < R_{OLR}$  and  $R_{OLR} < R < R_{OLR} + 1.5$  kpc, respectively). The same is true for variations of the parameter  $p_{max}$ : the pe-

riod of changes of  $p_{max}$  in the region of the inner ring is much shorter than in the region of the outer rings. Changes in the amplitude  $A_{max}$  in the region of the outer ring  $R_1$  ( $R_{-4/1} < R < R_{OLR}$ ) and in that of the outer ring  $R_2$  ( $R_{OLR} < R < R_{OLR} + 1.5$  kpc) are practically synchronized.

To a first approximation, the changes in the amplitude  $A_{max}$  and in the parameter  $p_{max}$  can be represented as cosine oscillations with a period  $P$  about the average value:

$$A_{max} = C_0 + C_1 \sin(2\pi t/P) + C_2 \cos(2\pi t/P), \quad (7)$$

$$p_{max} = D_0 + D_1 \sin(2\pi t/P) + D_2 \cos(2\pi t/P), \quad (8)$$

where  $C_0$  and  $D_0$  are average values,  $C_3 = \sqrt{C_1^2 + C_2^2}$  and  $D_3 = \sqrt{D_1^2 + D_2^2}$  are the amplitudes of oscillation, but  $\phi_a = \arctan(C_2/C_1)$  and  $\phi_p = \arctan(D_2/D_1)$  are the initial phases of oscillations of  $A_{max}$  and  $p_{max}$ , respectively.

We consider oscillations only starting from the time instant  $t = 0.5$  Gyr when the bar reaches its full strength. Eqs. 7 and 8 are linear with respect to the parameters  $C_0$ ,  $C_1$ ,  $C_2$ ,  $D_0$ ,  $D_1$ ,  $D_2$  and non-linear with respect to the oscillation period  $P$ . We have considered values of  $P$  in the range  $P \in [0.03, 5.0]$  Gyr with a step of 0.01 Gyr. For each value of  $P$ , the linear coefficients and the  $\chi^2$  function (the sum of squared normalized differences between the analytic representation, Eq. 7–8, and the observed values, Fig. 6) are calculated.

Fig. 7 (a) shows the  $\chi^2$  functions computed for model 1 in the region of the inner ring ( $R_{CR} < R < R_{-4/1}$ ). The  $\chi^2$  functions calculated from the analysis of oscillations of the parameter  $p_{max}$  (solid line) and of the amplitude  $A_{max}$  (dashed line) reach minimum values at  $P = 0.58 \pm 0.02$  and  $0.55 \pm 0.02$  Gyr, respectively. In the region of the inner ring the estimates of the period derived from the time series of  $A_{max}$  and  $p_{max}$  can be seen to agree well with each other.

The periods obtained for model 2 in the region of the inner ring derived from variations of  $p_{max}$  and  $A_{max}$  are  $0.58 \pm 0.02$  and  $P = 0.54 \pm 0.02$  Gyr, respectively.

Fig. 7 (b) shows the  $\chi^2$  functions computed for model 1 in the regions of the outer ring  $R_1$  ( $R_{-4/1} < R < R_{OLR}$ ) and the outer ring  $R_2$  ( $R_{OLR} < R < R_{OLR} + 1.5$  kpc). The  $\chi^2$  functions derived from the analysis of variations of the parameter  $p_{max}$  (solid lines) reach minimum values at  $P = 1.93 \pm 0.09$  ( $R_1$ ) and  $P = 2.00 \pm 0.09$  ( $R_2$ ) Gyr. The  $\chi^2$  functions calculated from the analysis of oscillations of the amplitude  $A_{max}$  (dashed lines) reach the local minimum at  $P = 0.96 \pm 0.02$  Gyr ( $R_1$ ) and  $P = 0.97 \pm 0.02$  Gyr ( $R_2$ ) followed by the local maximum and a sharp drop at  $P > 2.0$  Gyr.

The periods obtained for model 2 in the regions of the outer rings derived from variations of  $p_{max}$  and  $A_{max}$  have following values:  $P = 1.97 \pm 0.09$  ( $R_1$ ,  $p_{max}$ ),  $2.10 \pm 0.09$  ( $R_2$ ,  $p_{max}$ ),  $0.95 \pm 0.02$  ( $R_1$ ,  $A_{max}$ ), and  $1.00 \pm 0.02$  Gyr ( $R_2$ ,  $A_{max}$ ).

Thus, the corresponding values of the periods obtained for models 1 and 2 that differ by random deviations in the initial conditions coincide within the random errors. In the region of the inner ring, the period of oscillations of  $p_{max}$  and  $A_{max}$  is  $P = 0.57 \pm 0.02$  Gyr while in the region of the outer rings, the periods of oscillations are  $P = 2.0 \pm 0.1$  and  $0.97 \pm 0.02$  Gyr, respectively.

## 5 ORBITS SUPPORTING THE INNER COMBINED RING

### 5.1 Periods of oscillations of stars near the equilibrium points $L_4$ and $L_5$

Let us consider orbits near the Lagrange equilibrium points  $L_4$  and  $L_5$ . Fig. 8 shows examples of orbits near the stable equilibrium point  $L_4$  ( $L_5$ ). The initial coordinate  $X$  of the star is  $X(0) = 0$  (the star is located on the minor axis of the bar) and the initial radial velocity is  $V_R = 0$  in all four examples. The initial coordinate  $Y$  and the initial azimuthal velocity are indicated on the frames. For each star we also present the Jacobi integral,  $E_J$  (for more details, see section 6), which is conserved over the time interval  $t > T_g$  when the bar becomes time independent. Frame 8 (a) shows the orbit of a star located at the point  $L_4$  at the initial instant with the velocity equal to the velocity of the rotation curve  $V_c$  at the distance of the point  $L_4$ . The orbit resembles a small ellipse with the star moving clockwise (i.e. in the sense opposite that of galactic rotation). This is an example of a short-period orbit. Frames 8 (b, c, d) show some examples of a long-period orbit which resemble a banana.

We use the distribution of the potential in the model disc to calculate the periods of short- and long-period oscillations near the equilibrium point  $L_4$  ( $L_5$ ) and compare them with the periods of variations of  $A_{max}$  and  $p_{max}$  in the region of the inner ring.

Motions of stars in the reference frame of the bar rotating with the angular velocity  $\Omega_b$  are determined by the following equation:

$$\ddot{\mathbf{x}} = -\nabla\Phi_{\text{eff}} - 2\mathbf{\Omega}_b \times \dot{\mathbf{x}}, \quad (9)$$

where the coordinates  $\mathbf{x}$  and the velocities  $\dot{\mathbf{x}}$  characterize the motion in the rotating reference frame, the effective potential  $\Phi_{\text{eff}}$  includes both the gravitational potential and the potential of the centrifugal force:

$$\Phi_{\text{eff}} = \Phi - \frac{1}{2}\Omega_b^2 R^2, \quad (10)$$

and the term  $-2\mathbf{\Omega}_b \times \dot{\mathbf{x}}$  characterizes the contribution of the Coriolis force.

Let us consider the motion of stars relative to the equilibrium point  $L_4$  lying on the minor axis of the bar:

$$\xi = x - x_L, \quad (11)$$

$$\eta = y - y_L, \quad (12)$$

the coordinates  $\xi$  and  $\eta$  are measured along the major and minor axes of the bar, respectively. Expansion of  $\Phi_{\text{eff}}$  into Taylor series at the equilibrium point  $L_4$  and a consideration of the equilibrium condition:

$$\nabla\Phi_{\text{eff}}(L_4) = 0, \quad (13)$$

give us a possibility to write the equations of motion in the following form:

$$\ddot{\xi} = 2\Omega_b \dot{\eta} - \Phi_{xx}\xi, \quad (14)$$

$$\ddot{\eta} = -2\Omega_b \dot{\xi} - \Phi_{yy}\eta, \quad (15)$$

where the second derivatives  $\Phi_{xx}$  and  $\Phi_{yy}$  are taken at the equilibrium point  $L_4$ :

$$\Phi_{xx} = \frac{\partial^2 \Phi_{\text{eff}}}{\partial x^2}(L_4), \quad (16)$$

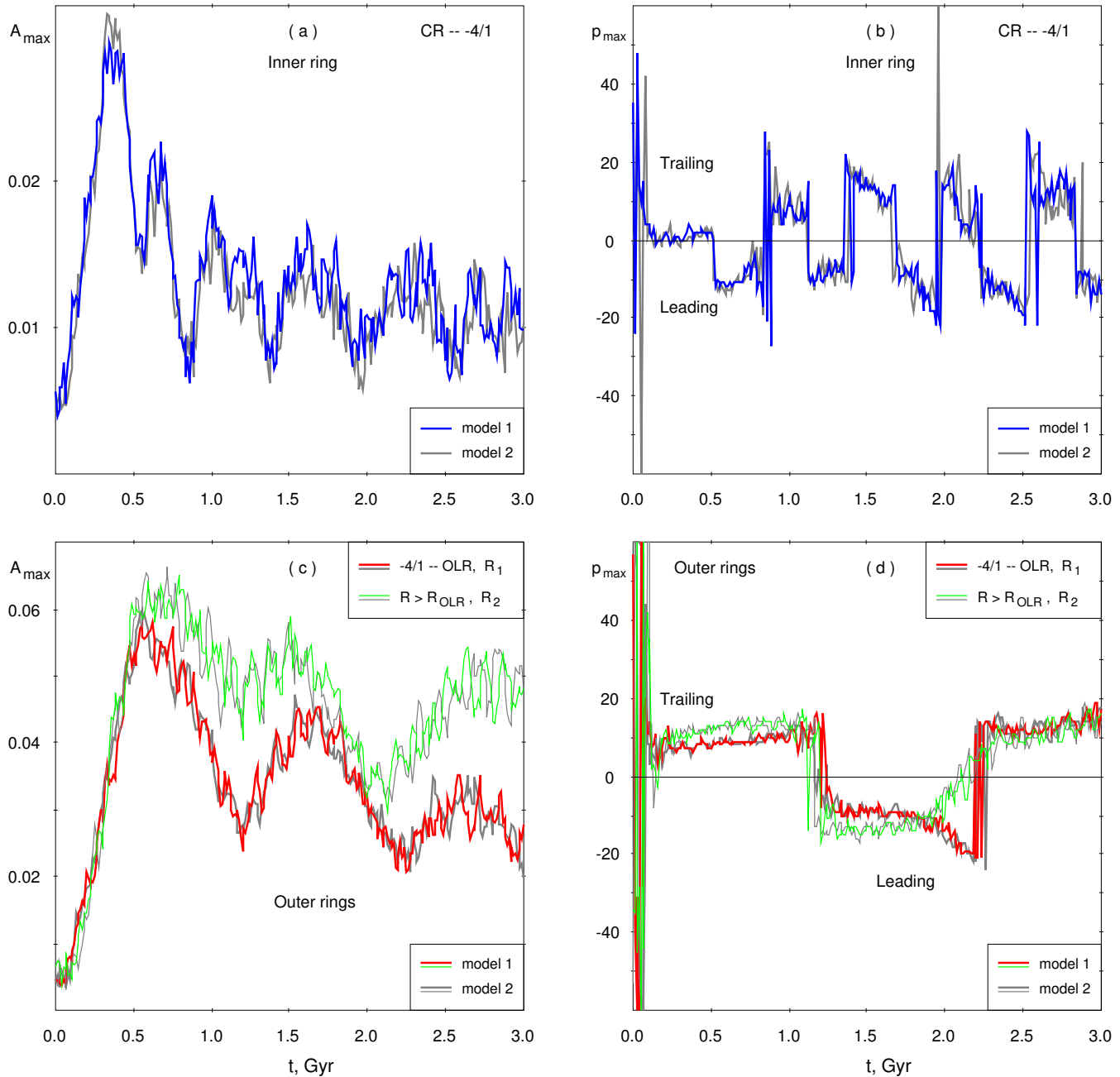


**Figure 6.** (a, c) Variations in maximum values,  $A_{max}$ , of the Fourier amplitude  $|A_2|$  calculated in the region of the inner ring (a) and the outer rings (c) as a function of time  $t$ . (b, d) Variations of the parameter  $p_{max} = -m/\tan\gamma$  corresponding to maximum value of the amplitude  $|A_2|$  computed in the region of the inner ring (b) and in the region of the outer rings (d) as a function of time. We can see that the parameters calculated for models 1 and 2 agree within the random fluctuations. The period of changes in the amplitude  $A_{max}$  in the regions of the inner ring (a) is much shorter than that in the region of the outer rings (c). Variations in  $A_{max}$  and  $p_{max}$  calculated in the region of the outer ring  $R_1$  ( $R_{-4/1} < R < R_{OLR}$ ) and in the region of the outer ring  $R_2$  ( $R_{OLR} < R < R_{OLR} + 1.5$  kpc) are practically synchronized.

$$\Phi_{yy} = \frac{\partial^2 \Phi_{\text{eff}}}{\partial y^2}(L_4). \quad (17)$$

Let us assume that a star oscillates about the equilibrium point  $L_4$  with the frequency  $\omega$ . Then we can write:

$$\xi = \xi_0 \exp(-i\omega t), \quad (18)$$

$$\eta = \eta_0 \exp(-i\omega t). \quad (19)$$

Substituting expressions Eq. 18–19 in the system of differential equations Eq. 14–15, we obtain a set of linear equations that has a non-trivial solution if its determinant is zero:

$$\omega^4 - (\Phi_{xx} + \Phi_{yy} + 4\Omega_b^2) \omega^2 + \Phi_{xx}\Phi_{yy} = 0. \quad (20)$$

The solution of this quadratic equation with respect to variable  $\omega^2$  has two different roots that characterize the frequency of motion of stars on long- and short-period or-

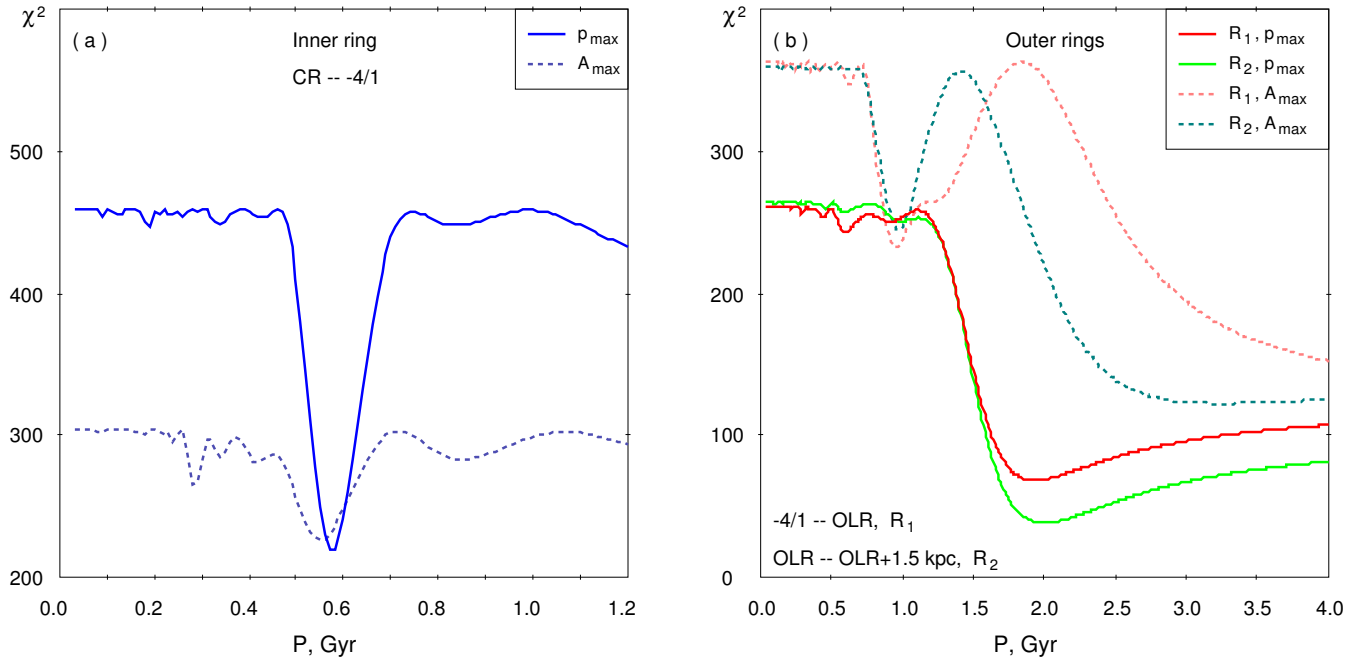


**Figure 7.** Dependences of the  $\chi^2$  values on the period  $P$  calculated for the parameter  $p_{max} = -m/\tan\gamma$  (solid lines) and for the amplitude  $A_{max}$  (dashed lines) in model 1. Functions  $\chi^2$  are calculated (a) in the region of the inner ring ( $R_{CR} < R < R_{-4/1}$ ) and (b) in the regions of the outer rings  $R_1$  and  $R_2$  ( $R_{-4/1} < R < R_{OLR}$  and  $R_{OLR} < R < R_{OLR} + 1.5$  kpc, respectively). (a) In the region of the inner ring, the  $\chi^2$  functions derived from the analysis of oscillations of the parameter  $p_{max}$  (solid line) and of the amplitude  $A_{max}$  (dashed line) reach their minimum values at  $P = 0.58 \pm 0.02$  and  $0.55 \pm 0.02$  Gyr, respectively. (b) In the region of the outer rings, the  $\chi^2$  functions derived from the analysis of oscillations of the parameter  $p_{max}$  (solid lines) reach their minimum values at  $P = 1.93 \pm 0.09$  Gyr ( $R_1$ ) and  $P = 2.00 \pm 0.09$  Gyr ( $R_2$ ); the  $\chi^2$  functions calculated from the analysis of the amplitude  $A_{max}$  (dashed lines) reach the local minima at  $P = 0.96 \pm 0.02$  Gyr ( $R_1$ ) and  $P = 0.97 \pm 0.02$  Gyr ( $R_2$ ) followed by the local maxima and a sharp drop at  $P > 2.0$  Gyr.

bits near the equilibrium point  $L_4$  (for more details, see Binney & Tremaine 2008, p. 178).

Table 1 lists the coordinates of the point  $L_4$  calculated from the equilibrium condition Eq. 13, the frequencies  $\omega_1$  and  $\omega_2$ , periods of motions on short- and long-period orbits, and their uncertainties, respectively.

The frequency of motions in short-period orbits practically coincides with the epicyclic frequency at the distance of the equilibrium point  $L_4$ , which is equal to  $\kappa = 0.0809$  Myr $^{-1}$ .

Note that the rotation period for long-period orbits,  $P = 565 \pm 2$  Myr (Table 1), agrees within the errors with the period found from the analysis of oscillations of  $p_{max}$  and  $A_{max}$  in the region of the inner ring,  $P = 570 \pm 20$  Gyr (section 4.2).

A possible explanation of the periodic enhancement of either leading or trailing segments of the inner ring is the presence of a mechanism which creates an overdensity in certain parts of banana-shaped orbits which then begins to circulate along a closed path, producing a density increase on either leading or trailing segments of banana-shaped orbits. Fig. 8 (d) illustrates such a possibility. We can see that the outer parts of banana-shaped orbits located outside the CR,  $R > R_{CR}$ , can be represented as a superposition of trailing and leading segments.

In general, we can even point the location where the overdensity forms. Fig. 6 (b) shows that oscillations start with the enhancement of leading segments of the inner ring which occurs during the time interval  $T \sim 0.52$ – $0.89$  Gyr, i.e.

just after the bar gains its full strength ( $T_g = 0.45$  Gyr). This means that at the time of the bar formation, the overdensity must be located at the top point of banana-shaped orbits, i.e. at the point farthest from the Galactic center. Then the overdensity begins to move clockwise which causes, in the first turn, the enhancement of leading segments of the inner ring.

To check this hypothesis, we selected stars located within a small circle at the time instant  $T_g = 0.45$  Gyr and traced their motion. Fig. 9 (a) shows the locations of the 6405 selected stars in the reference frame corotating with the bar at different time instants. At time  $T_g$ , the selected stars lie within the circle of the 200-pc radius with the center located on the minor axis of the bar at the distance of  $R = R_{CR} + 0.5$  kpc from the Galactic center (black points). The circular shape of the overdensity at the initial time instant is chosen only for simplicity. After  $1/4$  of the period  $P = 0.57$  Gyr, which determines the periodic changes of the morphology of the inner ring (section 4.2), the majority of the selected stars is shifted to the right with respect to the minor axis of the bar (green points). However, after  $3/4P$  from the instant  $T_g$ , the bulk of the selected stars is shifted to the left (red points). These displacements can be described with the use of the angle  $\varphi$  measured from the minor axis of the bar in the sense opposite that of the Galactic rotation,  $\varphi = \pi/2 - \theta$ . We calculated the median angle,  $\varphi_m$ , and median dispersion,  $\sigma_\varphi$ , (half of the central interval containing 68 per cent of objects) for the selected stars at different instants.

**Table 1.** Orbit periods near Lagrange points

L <sub>4</sub> (L <sub>5</sub> )	
$x_{L_4}$	0
$y_{L_4}$	$3.950 \pm 0.001$ kpc
$\omega_1$	$0.0803 \pm 0.0001$ Myr <sup>-1</sup>
$\omega_2$	$0.01111 \pm 0.00003$ Myr <sup>-1</sup>
$P_1$	$78.2 \pm 0.1$ Myr
$P_2$	$565 \pm 2$ Myr
L <sub>1</sub> (L <sub>2</sub> )	
$x_{L_1}$	$4.151 \pm 0.001$ kpc
$y_{L_1}$	0
$\omega_1$	$0.0794 \pm 0.0001$ Myr <sup>-1</sup>
$P_1$	$79.1 \pm 0.1$ Myr

Note that some of the selected stars appear not to be trapped by the banana-shaped orbits and continue their rotation around the Galactic center.

Fig. 9 (b) shows the oscillations of the median angle  $\varphi_m$  computed for the selected stars as a function of time. The angle  $\varphi_m$  varies in the range  $[-36, +38^\circ]$ , where the signs plus and minus correspond to the displacements to the right and to the left, respectively. Note that the amplitude of the oscillations of  $\varphi_m$  slowly decreases with time. The vertical lines show the  $+/-$  dispersion  $\sigma_\varphi$ , with the average  $\overline{\sigma_\varphi} = 27^\circ$ . Due to large number of stars in the overdensity, the average uncertainty in determination of  $\varphi_m$  is only  $\varepsilon_\varphi = 0.4^\circ$ . The green and red colours show the displacements for the instants  $t = T_g + (1/4 + n)P$  and  $t = T_g + (3/4 + n)P$  ( $n=0, \dots, 5$ ) when the bulk of the selected stars must achieve the extreme right and left positions, respectively. We can see that most of selected stars show oscillations relative to the minor axis of the bar and the period of  $P = 0.57 \pm 0.2$  Gyr describes these oscillations fairly well.

All these results support the hypothesis that the periodic changes in the morphology of the inner ring are due to the overdensity forming at the top point of banana-shaped orbits at the time  $T_g = 0.45$  Gyr, when the bar getting its full strength.

## 5.2 Orbits associated with the equilibrium points $L_1$ and $L_2$ and their contribution to the formation of the inner ring

Here we study the contribution of orbits associated with the unstable equilibrium points  $L_1$  and  $L_2$  to the formation of the inner ring.

We have found that the shape of stellar orbits which start their motion at the equilibrium points  $L_1$  and  $L_2$  depends on the way of the bar turning on: whether the bar exists from the very beginning or grows up slowly transforming from a round into elliptical structure in four bar rotation periods. Note that during the growth, the average radial force created by the bar conserves at any radius (Melnik et al. 2021).

Fig. 10 shows stellar orbits associated with the equilibrium points  $L_1$  and  $L_2$  obtained for the potential with non-axisymmetric perturbations of the bar existing from the very beginning (blue lines) and for the slowly growing bar (red

lines). The bar growth time is  $T_g = 0$  for the bar turning on instantly and  $T_g = 0.45$  Gyr for the slowly growing bar. The initial positions of all the stars considered coincide with the Lagrange equilibrium point  $L_1$ . The initial velocities of the stars are indicated on the frames. The initial conditions are the same for the two adjacent frames. For each star we present the Jacobi integral,  $E_J$ , which is conserved over the time interval  $t > T_g$ . During the bar growth the value of the Jacobi integral changes, namely, it increases.

Fig. 10 shows that orbits in the shape of 'lemon' (a, i), 'eight' (c), 'basket' (e) and 'flower' (g) obtained for the case of instant bar onset transform into banana-shaped orbits (b, d, f, h, j) when the bar turns on slowly. The periods of oscillations on banana-shaped orbits are  $P = 0.56-0.64$  Gyr, which are close but not exactly coincide with that of the long-period oscillations,  $P = 0.565 \pm 0.02$  Gyr (Table 1), around the equilibrium point  $L_4$ . All orbits shown in Fig. 10 support the inner ring.

A comparison with other studies of orbits in barred galaxies suggests that orbits in Fig. 10 (a, i) can be quasi-periodic ones forming around stable lemon-shaped orbits supporting the bar (Patsis et al. 2003, Figs 10 and 11 therein). The eight-shaped orbit in Fig. 10 (c) is similar to the unstable orbit with dimples in study by Contopoulos & Patsis (2006, Fig. 3c therein). The basket-shaped orbit in Fig. 10 (e) is similar to the chaotic orbits studied by Patsis et al. (2010, Fig. 14 therein) and Tsigaridi & Patsis (2013, Figs. 12-19 therein).

Orbits that resemble a 'lace' (Fig. 10 k, l) are of special case. Their shape depends little on the way the bar turns on. Note that 'lace' orbits are elongated in the direction perpendicular to the bar and partly lie outside the  $-4/1$  resonance, and hence they also support the outer ring  $R_1$  elongated perpendicular to the bar.

Fig. 10 shows that when the bar turns on slowly a great variety of orbits associated with the equilibrium points  $L_1$  and  $L_2$  transforms into banana-shaped orbits associated with the equilibrium points  $L_4$  and  $L_5$ .

A possible explanation of this behavior can be given in terms of resonance trapping (Chiba, Friske & Schönrich 2021; Chiba & Schönrich 2021, 2022). To be trapped by the Corotation Resonance, a star must lay in the so-called trapped region in the angle-action coordinates, which is bounded by the separatrix. If the bar changes its strength or angular velocity, the location of the separatrix also changes. The points  $L_1$  and  $L_2$  are always located outside the trapped region, so, in the case of instant bar onset, the orbit of a star, which starts its motion at the point  $L_1$ , always stay outside the trapped region (Fig. 10, left frames). However, when the bar turns on slowly, the Jacobi integral of the star changes and it has a chance to get inside the trapped region and be captured by the resonance (Fig. 10, right frames except 'lace' orbits).

Thus, in the case of slow bar onset, orbits associated with the unstable equilibrium points  $L_1$  and  $L_2$  can also support the inner combined ring.

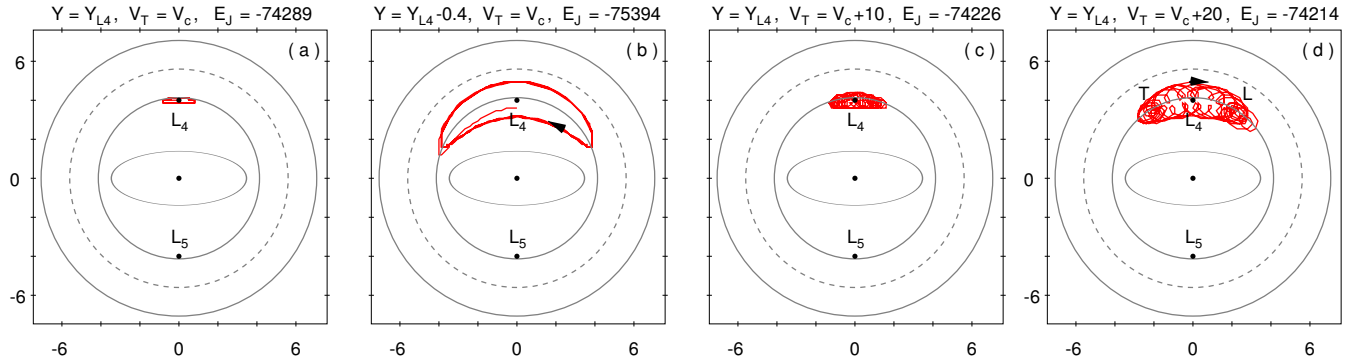


**Figure 8.** Some examples of orbits near the stable equilibrium point  $L_4$  ( $L_5$ ). All frames show orbits of stars with the initial coordinate  $X(0) = 0$  (the star is on the minor axis of the bar at  $t = 0$ ) and the initial radial velocity  $V_R = 0$ . The initial coordinate  $Y$  and the initial azimuthal velocity  $V_T$  are indicated on the frames. The velocity  $V_c$  is the velocity of the rotation curve at the distance of the point  $L_4$ . For each star we present the Jacobi integral,  $E_J$ , which is conserved over the time interval  $t > T_g$ . The additional velocities, coordinates, and Jacobi integrals are given in units of  $\text{km s}^{-1}$ , kpc, and  $\text{km}^2 \text{s}^{-2}$ , respectively. The position of the bar is shown by an ellipse. The gray solid lines indicate the CR and OLR, and the dashed line shows the resonance  $-4/1$ . Short-period orbits (SPO) are similar to small ellipses but long-period orbits (LPO) resemble a banana. Frame (d) also shows that the outer parts of banana-shaped orbits located outside the CR,  $R > R_{CR}$ , can be represented as a superposition of trailing and leading segments marked by the letters 'T' and 'L', respectively. The galaxy rotates counterclockwise. If an overdensity forms at some part of banana-shaped orbits, then it starts circulating the closed path causing the enhancement of either leading or trailing segments of the inner ring.

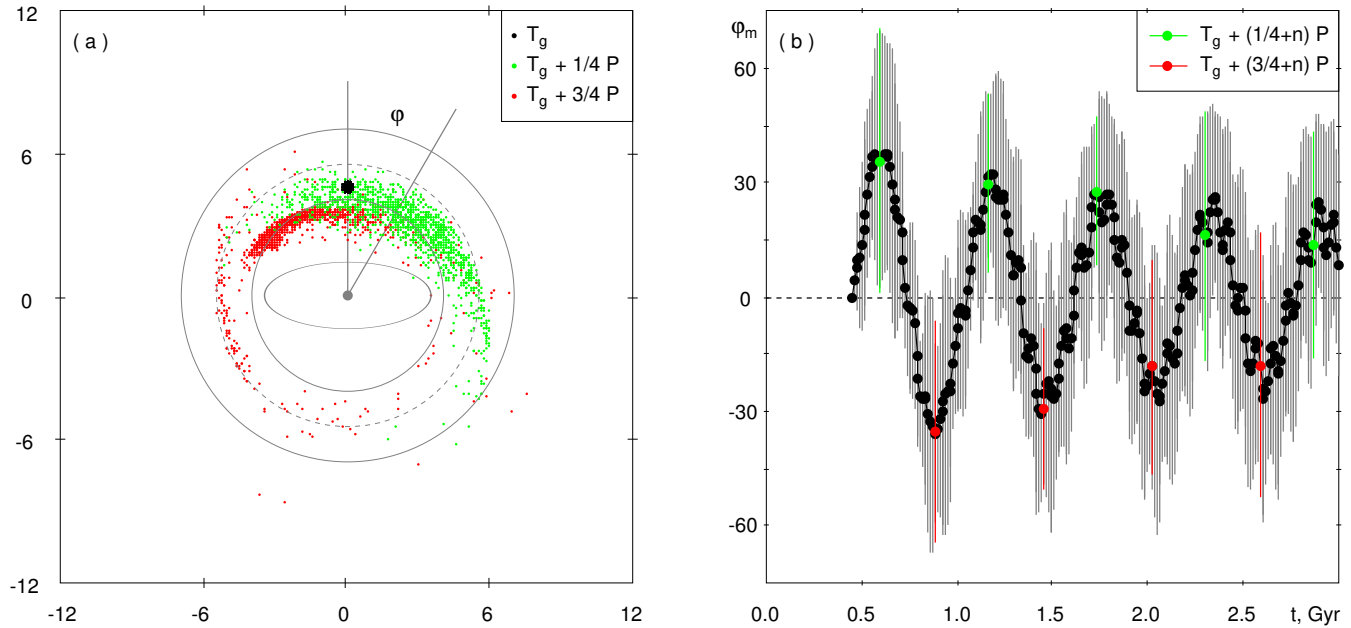


**Figure 9.** (a) Locations of the selected stars at different time instants. The selected stars are shown in the black, green, and red at the instants  $T_g$ ,  $T_g + 1/4P$ , and  $T_g + 3/4P$ , respectively, where  $P$  is close to the period of long-period oscillations,  $P = 0.57$  Gyr. We can see that most of the selected stars are shifted to the right and to the left with respect to the minor axis of the bar at the instants  $T_g + 1/4P$  and  $T_g + 3/4P$ , respectively. The angle  $\varphi$  is measured from the minor axis of the bar in the sense opposite to that of the Galactic rotation. The position of the bar is shown by an ellipse. The gray solid lines indicate the CR and OLR, and the dashed line – the resonance  $-4/1$ . (b) Oscillations of the median angle  $\varphi_m$  are computed for the selected stars as a function of time. The vertical lines indicate the  $\pm$  dispersion  $\sigma_\varphi$ . The green and red colours correspond to the instants  $t = T_g + (1/4 + n)P$  and  $t = T_g + (3/4 + n)P$ , where  $n=0\dots5$ , when the overdensity must achieve the extreme right and left positions, respectively. We can see that the majority of the selected stars demonstrates oscillations relative to the minor axis of the bar with the period of  $P = 0.57$  Gyr.

## 6 LIBRATION AND PRECESSION OF ORBITS NEAR THE OLR

In section 4.2 we showed that the periodic enhancement of either trailing or leading segments of the outer rings (oscillations of the parameter  $p_{max}$ ) occurs with the period of

$2.0 \pm 0.1$  Gyr. Let us consider an orbit which may be important for understanding the cause of these changes. Fig. 11 (a) shows the orbit of a star with the initial coordinates  $X(0) = 0$  and  $Y(0) = R_{OLR}$  and initial velocities  $V_R(0) = 0$  and  $V_T(0) = V_c$ , where  $V_c$  is the velocity of the rotation curve at the radius of the OLR. The orbit is considered in

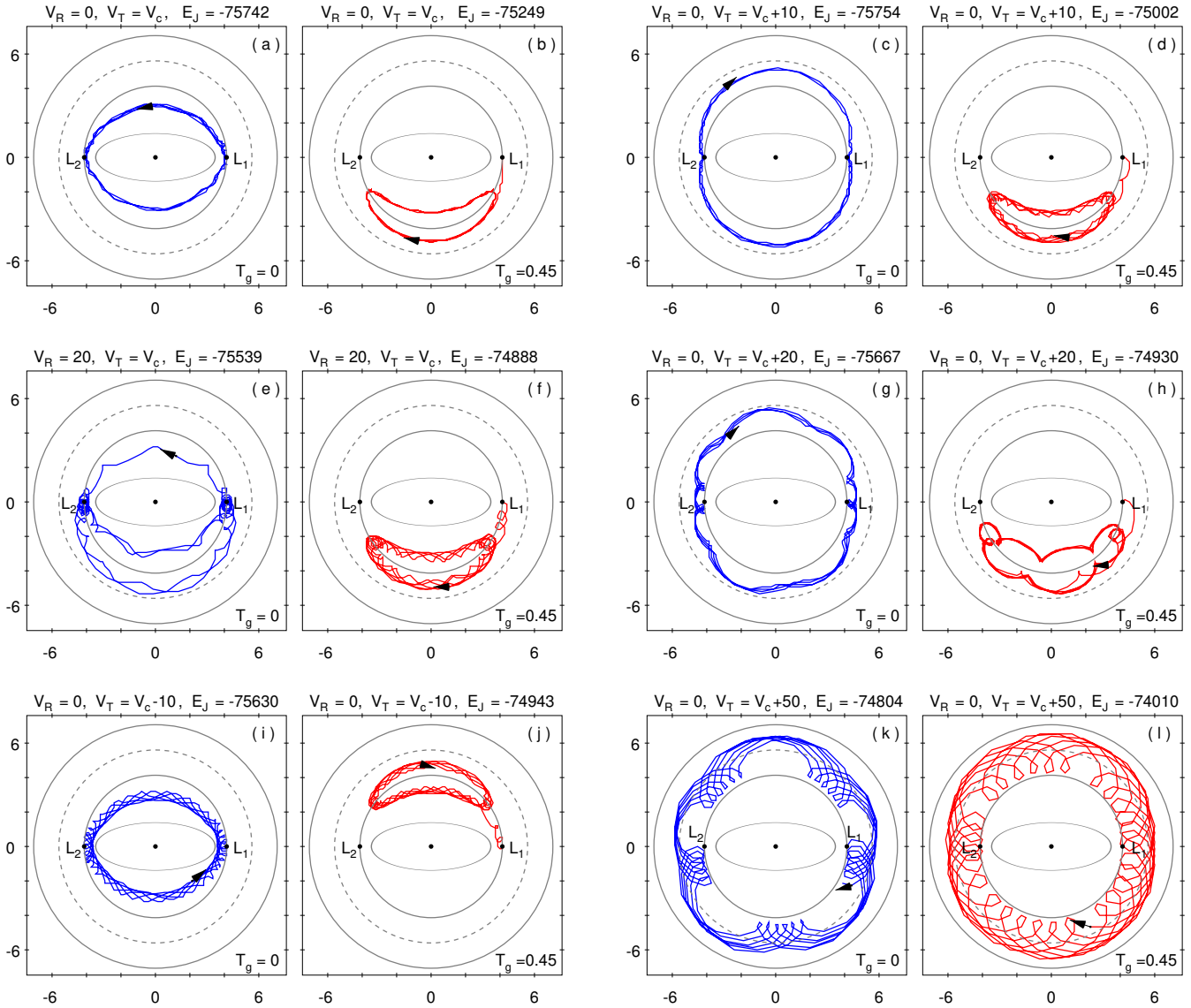


**Figure 10.** Stellar orbits associated with the equilibrium points  $L_1$  and  $L_2$  obtained for the potential with non-axisymmetric perturbations of the bar existing from the beginning of the simulation (blue orbits) and for the potential with slowly growing bar (red orbits). In the first case the growth time of the bar is  $T_g = 0$  while in the second case  $T_g = 0.45$  Gyr. The initial positions of all the stars coincide with the position of the Lagrange equilibrium point  $L_1$ . The initial velocities of the stars are indicated on the frames, where  $V_c$  is the velocity of the rotation curve at the distance  $L_1$ . For each star we present the Jacobi integral,  $E_J$ , which is conserved over the time interval  $t > T_g$ . The additional velocities, coordinates, and Jacobi integrals are given in units of  $\text{km s}^{-1}$ , kpc, and  $\text{km}^2 \text{s}^{-2}$ , respectively. The size of the frames is  $15 \times 15 \text{ kpc}^2$ . Two adjacent frames correspond to the same initial conditions. Orbits are shown in the reference frame of the rotating bar, therefore inside the CR stars move in the sense of the galactic rotation (counterclockwise) but outside the CR – in the opposite sense (clockwise). The gray solid lines indicate the CR and OLR, and the dashed line shows the resonance  $-4/1$ . We can see that the orbits in the shape of ‘lemon’ (a, i), ‘eight’ (c), ‘basket’ (e), and ‘flower’ (g) obtained for the bar turning on instantly transform into banana-shaped orbits (b, d, f, h, j) for the slowly growing bar. The shape of ‘lace’ orbits (k, l) depends little on the way the bar turns on. Both banana-shaped and ‘lace’ orbits support the inner ring. In addition, ‘lace’ orbits also support the outer ring  $R_1$ .

the reference frame of the rotating bar. We can see that in the time period 0–1 Gyr (green line) the direction of the orbit elongation is slightly inclined to the right relative to the minor axis of the bar, but in the time period 1–2 Gyr (red line) it is inclined to the left, and in the period 2–3 Gyr (dark blue line) the orbit returns to the original position (tilted to the right). When the orbit is inclined to the right (0–1, 2–3 Gyr), it supports the trailing segments of the rings

$R_1$  and  $R_2$ , but when it is inclined to the left (1–2 Gyr), it supports the leading segments of the outer rings.

Note that the orbits considered in this section were obtained for the bar that turns on slowly. However, this assumption is of no particular importance in the case of the outer rings: both bar onset scenarios result in nearly the same pattern of changes in the orientation of orbits.

Fig. 11 (a) also shows the supposed position of the Sun which lags behind the direction of the bar major axis by

the angle of  $\theta_b = 45^\circ$  (for more details, see Melnik et al. 2021). Note that the orbits inclined to the right (green and dark-blue lines) can cause the appearance of a large number of stars with large radial velocities directed away from the Galactic center in the solar vicinity which can appear and disappear in certain time periods.

Fig. 11 (b) shows the variations in the specific angular momentum  $L$  (red curve) of the star and in the specific total energy  $E = K + \Phi$  (blue curve) as a function of time, where  $K$  and  $\Phi$  are the specific kinetic and potential energy of the star, respectively. Since our model includes the isothermal halo, whose potential grows indefinitely at infinity, we introduced a constant into the formula for  $\Phi$ , for the potential energy at the distance  $R_{max}$  to be  $\Phi = 0$ . We integrate orbits up to the distance of 11 kpc and therefore we adopted  $R_{max} = 11$  kpc. We can clearly see the short-term and long-term oscillations of  $L$  and  $E$ . The short-term oscillations are due to the fact that a star twice in a period of a revolution around a bar gains and loses the angular momentum and energy from the bar. The periods of the short- and long-term oscillations are  $P = 0.13 \pm 0.01$  and  $1.91 \pm 0.01$  Gyr, respectively.

The presence of a bar rotating with the angular velocity  $\Omega_b$  in a galaxy leads to the fact that neither the angular momentum of a star  $L$  nor its energy  $E$  are conserved, the only quantity that is conserved is their combination in the form of the Jacobi integral:

$$E_J = E - \Omega_b L \quad (21)$$

(for example, Binney & Tremaine 2008). In our model, the Jacobi integral  $E_J$  at the distance of the OLR is conserved with a relative accuracy of  $10^{-5}$ .

Fig. 11 (b) shows that the star gradually, step by step, acquires angular momentum and energy from the bar and then also gradually loses them. Though our models are computed up to 3 Gyr, we integrated the orbits up to 6 Gyr to show that changes in  $L$ ,  $E$ , and other parameters are periodic.

Fig. 11 (c) shows the variations in the Galactocentric distance  $R$  of the star (red curve) and in its angular rotation velocity  $\dot{\theta}$  (blue curve). We can see that  $R$  and  $\dot{\theta}$  oscillate in anti-phase. Note that as the amplitude of oscillations increases, the average distance  $R$  also increases. In general, the pattern of oscillations resembles beats which arise in the case of a superposition of two oscillations with close frequencies. Near the resonance, we actually have two independent oscillation sources with close frequencies: the frequency with which a star meets the perturbation from the bar,  $2(\bar{\theta} - \Omega_b)$ , and the epicyclic frequency,  $\kappa$ . Formally, the beat frequency is defined by the following expression:

$$w_{bt} = \kappa(\bar{R}) + 2(\bar{\theta} - \Omega_b), \quad (22)$$

where the coefficient  $1/2$  is absent because of consideration the fact that the amplitude of the beats reaches extreme values twice per period. The 'plus' sign before  $\kappa$  is due to the fact that epicyclic motions occur in the sense opposite that of galactic rotation. The problem is that both  $\theta$  and  $\kappa$  depend on the distance  $R$ . Note that the beat frequency,  $w_{bt}$  (Eq. 22), is a particular case of the frequency of the resonance,  $\Omega_s$  (Eq. 2).

Is the epicyclic approximation valid for this orbit?

Fig. 11 (c) shows that the maximum amplitude of the radial oscillations of the star is 0.9 kpc. This value determines the maximum size of the epicycle in radial direction. Given that the average radius of the orbit is  $R = 7.2$  kpc, the size of the epicycle is about an order of magnitude smaller than the average radius of the orbit. It means that the epicyclic approximation is appropriate in this case.

Fig. 11 (e) shows variations in the average distance  $\bar{R}$  and in the average angular velocity  $\bar{\theta}$  as a function of time. Averaging was performed over the intervals of one oscillation along the radius: from one crossing of the radius  $R = R_{OLR}$  with the negative radial velocity,  $V_R < 0$ , to another. Fig. 11 (c) indicates that the star crosses this radius in each radial oscillation. The angular velocity  $\dot{\theta}$  was also averaged at the same intervals. Variations in  $\bar{R}$  and  $\bar{\theta}$  occur in the ranges of  $\bar{R} = 6.98\text{--}7.33$  kpc and  $\bar{\theta} = 30.73\text{--}32.33$  km s $^{-1}$  kpc $^{-1}$ , respectively. The period of changes is  $P = 1.91 \pm 0.01$  Gyr.

Fig. 11 (d) shows variations of the direction of orbit elongation ( $\theta_e$ , black circles) and eccentricity ( $e$ , gray circles) calculated at the intervals of one radial oscillation. Note that angle  $\theta_e$  is a particular case of the slow angle variable,  $\theta_s$  (Eq. 3). It can be clearly seen that the angle  $\theta_e$  changes non-uniformly: it lingers near  $+45^\circ$ , decreases fast at  $\theta_e = 0$ , and again lingers near  $-45^\circ$ . Then a fast orbital rearrangement occurs during which  $\theta_e$  jumps from  $-45^\circ$  to  $45^\circ$ . At this time the orbit has minimum eccentricity and minimum average radius  $\bar{R}$ . The angle  $\theta_e$  is measured from the major axis of the bar in the sense of Galactic rotation. Note that  $\theta_e = 0$  (orbit stretched in the direction of the bar major axis) corresponds to maximum average distance  $\bar{R}$ . When the angle  $\theta_e$  is near  $+45^\circ$ , the orbit is inclined to the right and supports the trailing segments of the outer rings, but when  $\theta_e$  is near  $-45^\circ$ , the orbit is inclined to the left and supports the leading segments of the outer elliptical rings. The changes in the angle  $\theta_e$  and the eccentricity of the orbit have periods of  $P = 1.95 \pm 0.04$  and  $P = 1.93 \pm 0.03$  Gyr, respectively. The eccentricity of the orbit varies in the range of 0.12–0.63.

The question is why  $\bar{R}$  reaches its maximum and does not increase further. This may be due to the orientation of the orbit at the time of maximum  $\bar{R}$ , when it becomes elongated along the major axis of the bar. At this orientation of the orbit, the bar begins to subtract effectively the angular momentum and energy from the star on the orbital segments located inside the OLR radius. This, in turn, causes a decrease in the average distance  $\bar{R}$  and a change in the orientation of the orbit. Note that the star at each radial oscillation is located both inside and outside the OLR radius which is seen well in Fig. 11c.

Struck (2015a) showed that the ratio of the epicyclic frequency to the angular velocity of the rotation curve:

$$M = \kappa/\Omega \quad (23)$$

depends on the eccentricity  $e$  of the orbit. For a flat rotation curve the relation between  $M_{cor}$  and  $M_0 = M(e = 0)$  has the following form:

$$M_{cor}/M_0 = 1.0013 - 0.00439x + 0.0520x^2 + 0.0169x^3 + 0.00180x^4, \quad (24)$$

where

$$x = \log_{10}(1 - e). \quad (25)$$



The correction that takes into account eccentricity slightly increases  $\kappa$ . The maximum correction for the orbit considered is obtained for the eccentricity  $e = 0.63$  and amounts to  $+0.51 \text{ km s}^{-1} \text{ kpc}^{-1}$ . It is small compared to the changes in  $\kappa$ ,  $\kappa = 43.60\text{--}45.89 \text{ km s}^{-1} \text{ kpc}^{-1}$ , caused by changes in the average distance  $\bar{R}$ .

Fig. 11 (f) shows variations in the angular velocity of the beats,  $w_{bt}$ . We used the average values of  $\bar{\theta}$  and  $\kappa(\bar{R})$  in our calculation of  $w_{bt}$  (Eq. 22). It can be seen that  $w_{bt}$  reverses the sign, but the values of  $w_{bt}$  are negative most of the time. Note that the frequency  $w_{bt}$  changes in anti-phase with the average distance  $\bar{R}$ . Considering the changes in  $w_{bt}$  as a time series, we obtain the period of  $P = 1.91 \pm 0.02$  Gyr.

Let us consider another orbit which demonstrates a variety of beat patterns in the OLR region. Fig. 12 (see Appendix) shows the orbit of a star with the initial coordinates  $X(0) = 0$  and  $Y(0) = R_{OLR}$  and initial velocities  $V_R(0) = 0$  and  $V_T(0) = V_c + 15 \text{ km s}^{-1}$ . It also shows variations in the angular momentum of the star  $L$ , total energy  $E$ , instantaneous values of the distance  $R$ , angular velocity  $\theta$ , eccentricity  $e$ , average distance  $\bar{R}$ , average angular velocity  $\bar{\theta}$ , and frequency of beats  $w_{bt}$  as a function of time. The averaging of  $\bar{R}$  and  $\bar{\theta}$  was performed over time intervals from one crossing of the radius  $R = R_{OLR} + 0.5 \text{ kpc}$  with a negative radial velocity to another.

Fig. 12 (e) shows that the direction of the orbit elongation  $\theta_e$  shifts from  $+90$  to  $-90^\circ$  at a nearly constant angular velocity. The elliptical orbit has the order of symmetry equal to  $m = 2$  and therefore we are dealing with the rotation of the direction of the orbit elongation or with the precession of the apsidal line. The period of the apsidal precession can be estimated from the long-term changes in the angular momentum and energy of the star which appears to be  $P = 0.81 \pm 0.01$  Gyr. In this case, the changes in the average distance  $\bar{R}$  are smaller and lie in the range  $\bar{R} = 7.46\text{--}7.56 \text{ kpc}$ . Note that most of the time the star is located only outside the OLR, but during the time periods when  $\bar{R}$  reaches maximum values, the star moves inside the OLR for short time intervals (Fig. 12 c). The eccentricity of the orbit changes only a little,  $\bar{e} = 0.42\text{--}0.52$ , maximum correction of  $\kappa$  due to orbital eccentricity is  $+0.32 \text{ km s}^{-1} \text{ kpc}^{-1}$  which is comparable to the range of changes in the epicycle frequency,  $\Delta\kappa = 0.63 \text{ km s}^{-1} \text{ kpc}^{-1}$ , caused by changes in  $\bar{R}$ . The estimates of the period derived from variations in the average distance  $\bar{R}$ , eccentricity, and beat frequency  $w_{bt}$  are also equal to  $P = 0.81 \pm 0.01$  Gyr.

The common feature of librating and precessing orbits is that they both lie inside and outside the OLR radius. The difference between librating and precessing orbits is in the restriction on angle  $\theta_e$ , whose variations are restricted for librating orbits and unrestricted for precessing ones (Weinberg 1994). In addition, we found that librating orbits are characterized by the reversal of the sign of the beat frequency,  $w_{bt}$ , during a period of oscillations while in the case of precessing orbits, the sign of  $w_{bt}$  remains unchanged. If  $w_{bt} > 0$  then the line of apsides rotates in the sense of galactic rotation and if  $w_{bt} < 0$ , in the opposite sense. A consequence of this feature is that librating orbits have longer oscillation periods than precessing orbits.

Among orbits that lie both inside and outside the OLR

in our model, the fractions of librating orbits is only 19 per cent, but a maximum in the distribution of librating orbits over the period corresponds to  $P = 1.9$  Gyr, and the fraction of librating orbits with the period in the range 1.8–2.0 Gyr amounts to  $\sim 60$  per cent. Thus, our model includes a sufficient number of orbits with the oscillation period of  $\sim 1.9$  Gyr.

## 7 DISCUSSION AND CONCLUSIONS

We studied the periodic changes in the morphology of the resonance rings using the dynamical model of the Galaxy which reproduces well the distribution of observed velocities derived from the *Gaia* EDR3 and *Gaia* DR3 catalogues along the Galactocentric distance. The velocities calculated for the *Gaia* EDR3 and *Gaia* DR3 data are consistent, on average, within  $1 \text{ km s}^{-1}$ .

We suppose that a sharp drop in the distribution of the azimuthal velocity  $V_T$  at  $R \approx 4.0\text{--}5.5 \text{ kpc}$  (Fig. 1 c) can be due to extinction, which acts differently on thin-disc, thick-disc, and halo stars. Note that the spiral distribution (snail shell) of azimuthal velocities  $V_T$  of *Gaia* DR2 and *Gaia* DR3 stars in the  $(Z, V_Z)$  plane, which many authors attribute to perturbations from the dwarf galaxy Sgr dSph (Antoja et al. 2018, 2023), can be due to similar effects.

The model disc forms the nuclear ring, inner combined ring, and outer resonance rings  $R_1$  and  $R_2$  (Fig. 2).

We demonstrated that the periodic changes in the ring morphology are not due to random deviations in the initial distributions of the density and velocity (Fig. 6).

The inner ring is located in the region between the CR (4.0 kpc) and the resonance  $-4/1$  (5.5 kpc). This ring is not like other resonance rings where stars make a complete revolution around the Galactic center. The identified inner ring can be called a combined feature: stars move along banana-type orbits near the stable equilibrium points  $L_4$  and  $L_5$ . We have found a density increase on either trailing or leading segments of the inner ring with a period of  $P = 0.57 \pm 0.02$  Gyr (Fig. 6 a, b). The period of a revolution of stars in long-period orbits near the equilibrium point  $L_4$  ( $L_5$ ) is  $P = 0.565 \pm 0.002$  Gyr, which is very close to the period of morphological changes in the inner ring.

A possible explanation of periodic enhancement of either leading or trailing segments of the inner ring is the presence of the overdensity, which forms at the top point of banana-shaped orbits when the bar reaches its full strength and then begins circulating along the closed contour (Fig. 9).

Orbits associated with the unstable equilibrium points  $L_1$  and  $L_2$  also support the inner combined ring (in agreement with Athanassoula et al. 2009b). Orbits associated with the unstable equilibrium points  $L_1$  and  $L_2$  also support the inner combined ring. In the case of slow bar onset a great variety of orbits associated with the equilibrium points  $L_1$  and  $L_2$  transforms into banana-shaped orbits (Fig. 10).

How would we classify the inner combined ring, if we could have seen our Galaxy from the outside? Perhaps we would classify it as an outer lens  $L$ , which surrounds the bar like a rim. Buta & Combes (1996, Table 7 therein) found that the outer lenses are elongated perpendicular to the bar in 74 per cent cases of galaxies considered.

The mechanisms causing the morphological changes

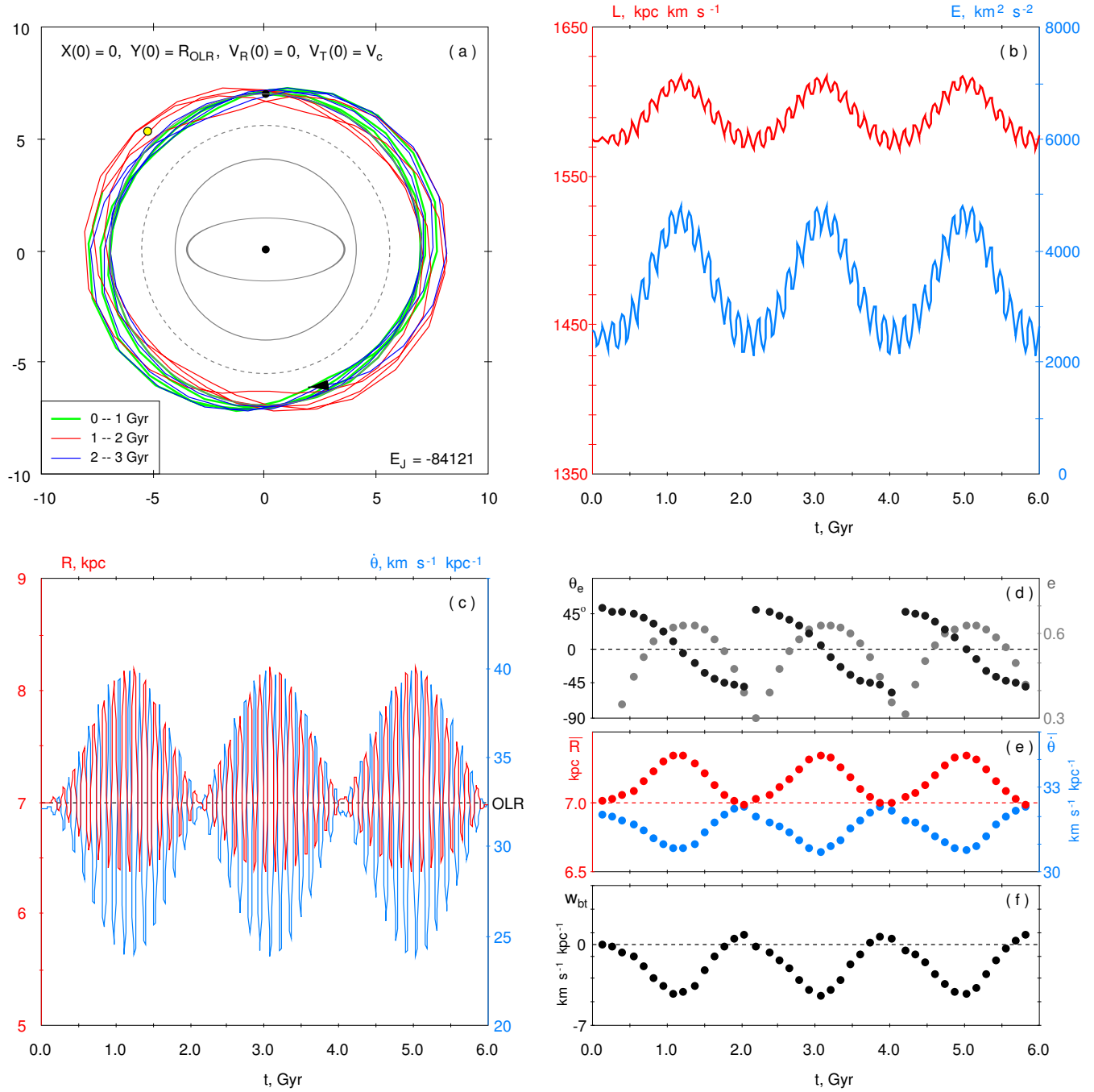


**Figure 11.** (a) Orbit of the star with the initial coordinates  $X(0) = 0$  and  $Y(0) = R_{OLR}$  and initial velocities  $V_R(0) = 0$  and  $V_T(0) = V_c$  in the reference frame of the rotating bar. Also shown is the Jacobi integral,  $E_J$ , related to the time interval  $t > T_g$ . The black and yellow circles indicate the initial position of the star and the supposed position of the Sun, respectively. The segments of the orbit for the time periods 0–1, 1–2, and 2–3 Gyr are shown in green, red, and dark-blue, respectively. The Galaxy rotates counterclockwise. The arrow indicates the sense of rotation of the star in the bar reference frame. The position of the bar is shown by an ellipse. The gray solid lines indicate the CR and OLR, and the dashed line, the resonance  $-4/1$ . We can see that the direction of orbit elongation is slightly inclined to the right relative to the minor axis of the bar during the time period 0–1 (green line), but it is inclined to the left during the period 1–2 Gyr (red line), and the orientation of the orbit returns to the initial position (tilted to the right) during the period 2–3 Gyr (dark-blue line). (b) Variations in the angular momentum  $L$  of the star (red curve) and in the total energy  $E$  (blue curve) as a function of time. The left and right vertical axes show the scales of changes in  $L$  and  $E$ , respectively. We can clearly see short- and long-term oscillations in  $L$  and  $E$ . Long-term oscillations have the period of  $P = 1.91 \pm 0.01$  Gyr. (c) Variations in the Galactocentric distance of the star  $R$  (red curve) and in its instantaneous angular velocity  $\dot{\theta}$  (blue curve) as functions of time. The scales of changes in  $R$  and  $\dot{\theta}$  are shown on the left and right axes, respectively. It can be clearly seen that oscillations in  $R$  and  $\dot{\theta}$  occur in anti-phase. The horizontal dashed line indicates the position of the OLR. (d) Variations in the direction of the orbit elongation ( $\theta_e$ , black dots, left vertical axis), and in the eccentricity of the orbit ( $e$ , gray dots, right vertical axis). The angle  $\theta_e$  is measured from the major axis of the bar and increases in the sense of Galactic rotation. (e) Variations in the average values of  $\bar{R}$  and  $\bar{\theta}$ . (f) Variations in the beat frequency  $w_{bt}$ .

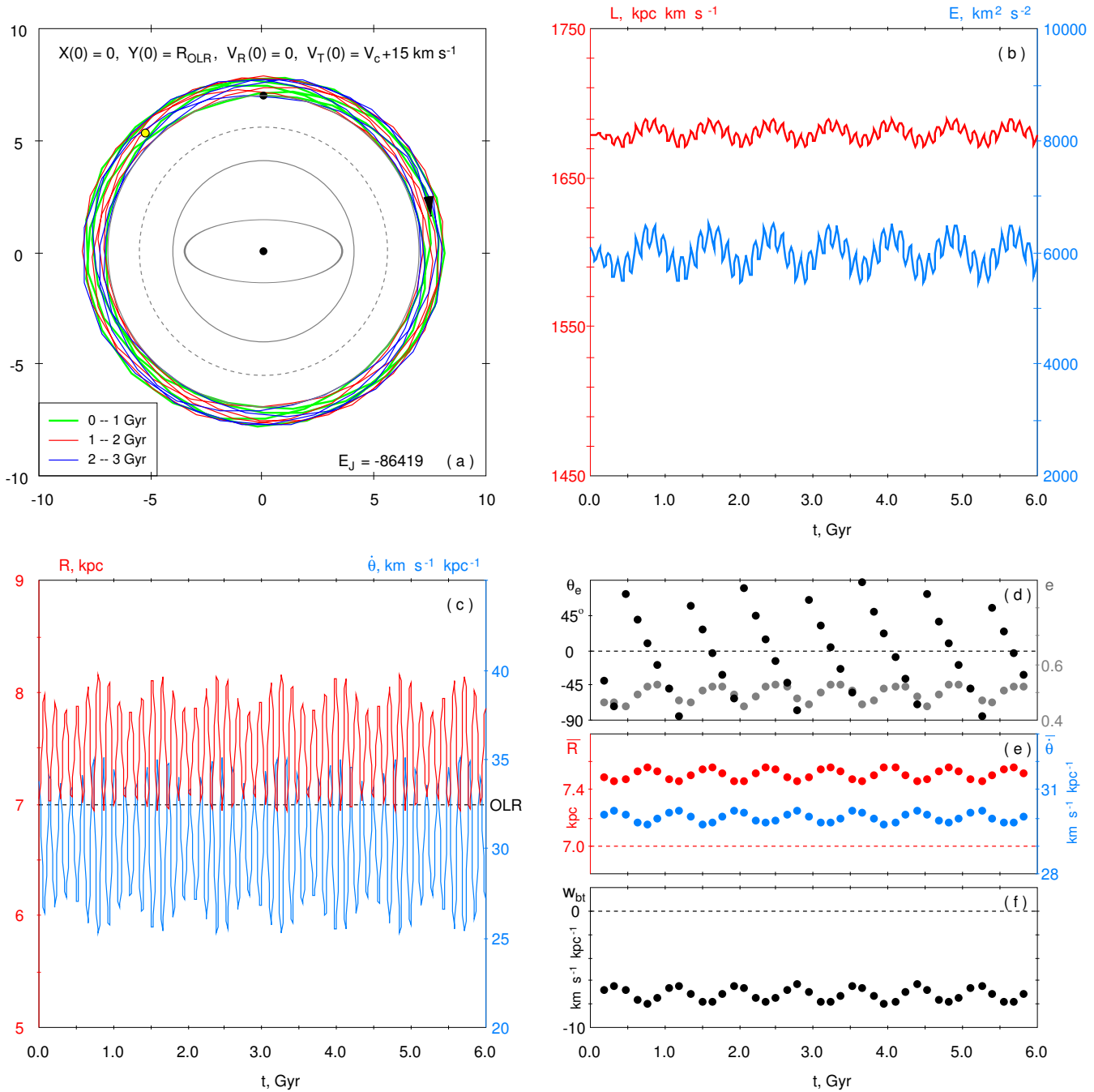


**Figure 12.** (a) Orbit of the star with the initial coordinates  $X(0) = 0$  and  $Y(0) = R_{OLR}$  and velocities  $V_R(0) = 0$  and  $V_T(0) = V_c + 15 \text{ km s}^{-1}$  in the reference frame of the rotating bar. Also shown is the Jacobi integral,  $E_J$ . (b) Changes in the angular momentum of the star ( $L$ , red curve) and in the total energy ( $E$ , blue curve) as functions of time. Long-term oscillations in  $L$  and  $E$  have a period of  $P = 0.81 \pm 0.01 \text{ Gyr}$ . (c) Variations in the distance of the star ( $R$ , red curve) and in its angular rotation velocity ( $\dot{\theta}$ , blue curve) as functions of time. The horizontal dashed line indicates the position of the OLR. (d) Variations in the direction of the orbit elongation,  $\theta_e$ , and eccentricity. It can be observed that angle  $\theta_e$  shifts nearly uniformly with time. (e) Variations of average  $\bar{R}$  and  $\bar{\theta}$ . (f) Variations of the beat frequency  $w_{bt}$ . Note that  $w_{bt}$  takes only negative values. For more details, see caption to Fig. 11.

near the CR and near the OLR are different. Near the CR we observe librations of stars along banana-shaped orbits, but orbits themselves do not librate, so we need overdensity to explain morphological changes here. However, near the OLR we observe librations of orbits, so there is no need for overdensity there.

In the region of the outer rings, we have found periodic

enhancement of either leading or trailing segments of the outer rings with a period of  $P = 2.0 \pm 0.1 \text{ Gyr}$  (Fig. 6 c, d). We studied orbits in the vicinity of the OLR and found oscillations of the direction of orbit elongation, which seem to be due to the beats between the frequency with which a star meets perturbations from the bar,  $2(\Omega - \Omega_b)$ , and

the epicyclic frequency  $\kappa$ . The beat frequency (Eq. 22) is a particular case of the frequency of the resonance (Eq. 2).

Among many oscillating orbits, we have discovered those with the oscillation period of  $P = 1.91 \pm 0.01$  Gyr. If the orbit is inclined in the sense opposite that of Galactic rotation (to the right in Fig. 11), it supports the trailing segments of the rings  $R_1$  and  $R_2$ , but if it is tilted in the sense of Galactic rotation (to the left in Fig. 11), it supports the leading segments of the rings. It may be just these orbits ( $P \approx 1.9$  Gyr) that cause the enhancement of either trailing or leading segments of the outer rings with the period of  $P = 2.0 \pm 0.1$  Gyr.

Oscillations in the orientation of the orbits are also accompanied by long-term oscillations of the angular momentum  $L$ , energy  $E$ , average distance  $\bar{R}$ , average angular velocity  $\bar{\theta}$ , eccentricity  $e$ , and beat frequency  $w_{bt}$  (Eq. 22). Oscillations of these parameters have the same periods. Maxima of the average distance  $\bar{R}$  correspond to maxima of  $L$ ,  $E$ , and eccentricity  $e$ , as well as to minima of the average angular velocity  $\bar{\theta}$  and beat frequency  $w_{bt}$  (Fig. 11).

Among many factors that determine the oscillation period, it is worth emphasizing the closeness of the average radius of the orbit to the radius of the OLR.

The angle  $\theta_e$  determines the direction of orbit elongation with respect to the major axis of the bar and increases in the sense of Galactic rotation. The orbit with the oscillation period of  $P = 1.91 \pm 0.01$  Gyr exhibits non-uniform variations of the angle  $\theta_e$ : it decreases slowly near  $+45^\circ$ , decreases rapidly near  $\theta_e = 0$ , and again decreases slowly near  $-45^\circ$ , and then a fast rearrangement of the orbit occurs during which  $\theta_e$  jumps from  $-45^\circ$  to  $45^\circ$ . Note that during the orbital rearrangement, the average size of the orbit  $\bar{R}$  and its eccentricity have minimum values.

Note that the period of oscillations of the maximum value,  $A_{max}$ , of the Fourier amplitude  $|A_2|$  is  $P = 0.97 \pm 0.02$  Gyr, which is approximately half of the oscillation period of the parameter  $p_{max} = -m/\tan \gamma$  equal to  $P = 2.0 \pm 0.1$  Gyr (Fig. 7 b). Oscillations in the amplitude  $A_{max}$  may be due to oscillations in the orientation of the orbit: when it is elongated at the angle  $\theta_e \approx 45^\circ$  ( $\theta_e \approx -45^\circ$ ) it makes bridges between the trailing (leading) segments of the rings  $R_1$  and  $R_2$ , which causes trailing (leading) spiral arms to become longer which, in its turn, must increase the value of  $A_{max}$ . Angle  $\theta_e$  takes values of  $\pm 45^\circ$  twice per period and therefore the oscillation period of  $A_{max}$  must be nearly twice shorter than that of  $\theta_e$ , which is equal to  $P = 1.95 \pm 0.04$  Gyr.

Among orbits that lie both inside and outside the OLR in our model, the fractions of librating and precessing orbits are 19 and 75 per cent, respectively. Besides, 5 and 1 per cent of orbits considered oscillate within  $\pm 15^\circ$  with respect to the major and minor axes of the bar, respectively. Note that a maximum in the distribution of librating orbits over the period corresponds to the value of  $P = 1.9$  Gyr, and the fraction of librating orbits with the periods in the range 1.8–2.0 Gyr amounts to  $\sim 60$  per cent. Thus, our model includes a sufficient number of orbits with the oscillation period of  $\sim 1.9$  Gyr.

A clearer understanding of the frequency distribution of the oscillation periods requires an additional study that goes beyond the scope of this work.

## 8 ACKNOWLEDGEMENTS

We thank the anonymous editor and referee for fruitful discussion especially in part concerning orbits in barred galaxies. We thank Ralph Schönrich for his remarks and suggestions concerning orbits in the case of instant and slow bar onset (section 5.2). This work has made use of data from the European Space Agency (ESA) mission *Gaia* (<https://www.cosmos.esa.int/gaia>), processed by the *Gaia* Data Processing and Analysis Consortium (DPAC, <https://www.cosmos.esa.int/web/gaia/dpac/consortium>). Funding for the DPAC has been provided by national institutions, in particular the institutions participating in the *Gaia* Multilateral Agreement. E.N. Podzolkova is a scholarship holder of the Foundation for the Advancement of Theoretical Physics and Mathematics "BASIS" (Grant No. 21-2-2-44-1).

## 9 DATA AVAILABILITY

The data underlying this article were derived from sources in the public domain: Vizier at <https://vizier.u-strasbg.fr/viz-bin/VizieR>

## REFERENCES

- Antoja T., Helmi A., Romero-Gomez M. et al., 2018, *Nature*, 561, 360
- Antoja, T., Ramos, P., Garcia-Conde, B., Bernet, M., Laporte, C. F. P., Katz, D. 2023, *A&A*, 673, A115
- Athanassoula E. 1992a, *MNRAS*, 259, 328
- Athanassoula E. 1992b, *MNRAS*, 259, 345
- Athanassoula, E., Bienayme, O., Martinet, L., Pfenniger, D. 1983, *A&A*, 127, 349
- Athanassoula, E., Bosma, A., Crézé, M., Schwarz, M. P. 1982, *A&A*, 107, 101
- Athanassoula, E., Romero-Gómez, M., Bosma, A., Masdemont, J. J. 2009b, *MNRAS*, 400, 1706
- Athanassoula, E., Romero-Gómez, M., Bosma, A., Masdemont, J. J. 2010, *MNRAS*, 407, 1433
- Athanassoula, E., Romero-Gómez, M., Masdemont, J. J. 2009a, *MNRAS*, 394, 67
- Barbanis, B. 1970, *IAU Symp.* 38, 343, Dordrecht, Reidel
- Benjamin, R. A., Churchwell, E., Babler, B. L., et al. 2005, *ApJ*, 630, L149
- Binney, J., Tremaine, S., *Galactic Dynamics*, Second Edition, Princeton Univ. Press, Princeton, New Jersey, 2008.
- Block, D. L., Puerari, I., Knapen, J. H., et al., 2001, *A&A*, 375, 761
- Boehle, A., Ghez, A. M., Schödel, R. et al. 2016, *ApJ*, 830, 17
- Branham, R. L. 2017, *Ap&SS*, 362, 29
- Buta, R. 1995, *ApJS*, 96, 39
- Buta, R. 2017, *MNRAS*, 471, 4027
- Buta, R., Combes, F. 1996, *Fund. Cosmic Physics*, 17, 95
- Buta, R., Crocker, D. A. 1991, *AJ*, 102, 1715
- Buta, R., Laurikainen, E., Salo, H. 2004, *AJ*, 127, 279
- Byrd, G., Rautiainen, P., Salo, H., Buta, R., Crocker, D. A. 1994, *AJ*, 108, 476
- Cabrera-Lavers, A., Hammersley, P. L., González-Fernández, C., et al. 2007, *A&A*, 465, 825
- Chiba, R., Friske, J., Schönrich, R. 2021, *MNRAS*, 500, 4710

- Chiba, R., Schönrich, R. 2021, MNRAS, 505, 2412
- Chiba, R., Schönrich, R. 2022, MNRAS, 513, 768
- Churchwell, E., Babler, B. L., Meade, M. R., et al. 2009, PASP, 121, 213
- Comerón, S., Salo, H., Laurikainen, E., et al. 2014, A&A, 562, 121
- Considerere, S., Athanassoula, E. 1982, A&A, 111, 28
- Contopoulos, G. 1978, A&A, 64, 323
- Contopoulos, G. 1983, Celest. Mechan., 31, 193
- Contopoulos, G. in *Chaos in Astronomy*, Astrophysics and Space Science Proceedings, ed. by G. Contopoulos and P. A. Patsis, Springer-Verlag Berlin Heidelberg, 2009, p. 1
- Contopoulos, G., Harsoula, M. 2010, Celest. Mechan. and Dynamic. Astron., 107, 77
- Contopoulos, G., Grosbol, P. 1989, A&AR, 1, 261
- Contopoulos, G., Papayannopoulos, Th. 1980, A&A, 92, 33
- Contopoulos, G., Patsis, P. A. 2006, MNRAS, 369, 1039
- Dambis, A. K., Berdnikov, L. N., Kniazev, A. Y., et al. 2013, MNRAS, 435, 3206
- Danby, J. M. 1965, AJ, 70, 501
- de Vaucouleurs, G., Freeman, K. C. 1972, Vis. in Astron., 14, 163
- Díaz-García, S., Salo, H., Laurikainen, E., Herrera-Endoqui, M. 2016, A&A, 587, 160
- Dwek, E., Arendt, R. G., Hauser, M. G., et al. 1995, ApJ, 445, 716
- Eisenhauer, F., Genzel, R., Alexander, T., et al. 2005, ApJ, 628, 246
- Feast, M. W., Laney, C. D., Kinman, T. D., van Leeuwen, F., Whitelock, P. A. 2008, MNRAS, 386, 2115
- Francis, Ch., Anderson, E. 2014, MNRAS, 441, 1105
- Fujii, M. S., Bédorf, J., Baba, J., Portegies Zwart, S. 2019, MNRAS, 482, 1983
- Fux, R. 2001, A&A 373, 511
- Gaia Collaboration, Brown, A. G. A., Vallenari, A., et al. 2018, A&A, 616, A1
- Gaia Collaboration, Brown, A. G. A., Vallenari, A., et al. 2021, A&A, 649, A1
- Gaia Collaboration, Katz, D., Antoja, T., et al. 2018, A&A, 616, A11
- Gaia Collaboration, Prusti, T., de Bruijne, J. H. J., et al. 2016, A&A, 595, A1
- Gaia Collaboration, Vallenari, A., Brown, A. G. A., et al. 2023, A&A, 674, A1
- Gerhard, O. 2011, Mem. S. A. It. Suppl., 18, 185
- Glushkova, E. V., Dambis, A. K., Melnik, A. M., Rastorguev, A. S. 1998, A&A, 329, 514
- González-Fernández, C., López-Corredoira, M., Amôres, E. B., Minniti, D., Lucas, P., Toledo, I. 2012, A&A, 546, 107
- Groenewegen, M. A. T., Udalski, A., Bono, G. 2008, A&A, 481, 441
- Iwanek, P., Poleski, R., Kozłowski, S., et al. 2023, ApJS, 264, 20
- Kalnajs, A. J. 1971, ApJ, 166, 275
- Katz, D., Sartoretti, P., Cropper, M., et al. 2019, A&A, 622, A205
- Kormendy, J. 1979, ApJ, 227, 714
- Laurikainen, E., Salo, H., Buta, R., Knapen, J. H. 2011, MNRAS, 418, 1452
- Lindgren, L., Klioner, S. A., Hernandez, J., et al. 2021, A&A, 649, A2
- Marshall, D. J., Robin, A. C., Reyle, C., Schultheis, M., Picaud, S. 2006, A&A, 453, 635
- Melnik, A. M. 2019, MNRAS, 485, 2106
- Melnik, A. M., Dambis, A. K., Podzolkova, E. N., Berdnikov, L. N. 2021, MNRAS, 507, 4409
- Melnik, A. M., Rautiainen, P. 2009, Astron. Lett., 35, 609
- Melnik, A. M., Rautiainen, P. 2011, MNRAS, 418, 2508
- Melnik, A. M., Rautiainen, P. 2013, MNRAS, 434, 1362
- Melnik, A. M., Rautiainen, P., Berdnikov, L. N., Dambis, A. K., Rastorguev, A. S. 2015, AN, 336, 70
- Melnik, A. M., Rautiainen, P., Glushkova, E. V., Dambis, A. K. 2016, Ap&SS, 361, 60
- Monari, G., Famaey, B., Siebert, A., Duchateau, A., Lorscheider, T., Bienayme, O. 2017, MNRAS, 465, 1443
- Mühlbauer, G., Dehnen, W. 2003, A&A, 401, 975
- Nataf D. M. 2017, PASA, 34, 41
- Neckel, Th., Klare, G. 1980, ApJS, 42, 251
- Ness, M., Lang, D. 2016, AJ, 152, 14
- Nikiforov, I. I. 2004, ASP Conf. Ser. Vol. 316, Astron. Soc. Pac., San Francisco, p. 199
- Nishiyama, S., Nagata, T., Sato, S., et al. 2006, ApJ, 647, 1093
- Patsis, P. A., Kalapotharakos, C., Grosbol, P. 2010, MNRAS, 408, 22
- Patsis, P. A., Skokos, Ch., Athanassoula, E. 2003, MNRAS, 346, 1031
- Patsis, P. A., Tsigaridi, L. 2017, Ap&SS, 362, 129
- Pfenniger, D. 1984, A&A, 134, 373
- Rautiainen, P., Melnik, A. M. 2010, A&A, 519, 70
- Rautiainen, P., Salo, H. 1999, A&A, 348, 737
- Rautiainen, P., Salo, H. 2000, A&A, 362, 465
- Reid, M. J., Menten, K. M., Zheng, X. W., Brunthaler, A., Xu, Y. 2009, ApJ, 705, 1548
- Rodriguez-Fernandez, N. J., Combes, F. 2008, A&A, 489, 115
- Sartoretti, P., Katz, D., Cropper, M., et al. 2018, A&A, 616 A6
- Schwarz, M. P. 1981, ApJ, 247, 77
- Sellwood, J. A., Wilkinson, A. 1993, Rep. on Prog. in Phys., 56, 173
- Shen, J., Rich, R. M., Kormendy, J., et al. 2010, ApJ, 720, L72
- Simion, I. T., Belokurov, V., Irwin, M., et al. 2017, MNRAS, 471, 4323
- Sormani M. C., Sobacchi E., Fragkoudi F., et al. 2018, MNRAS, 481, 2
- Struck, C. 2015, MNRAS, 446, 3139
- Struck, C. 2015, MNRAS, 450, 2217
- Trick, W. H., Fragkoudi, F., Hunt, J. A. S., Mackereth, J. T., White, S. D. M. 2021, MNRAS, 500, 2645
- Tsigaridi, L., Patsis, P. A. 2013, MNRAS, 434, 2922
- Weinberg, M. D. 1994, ApJ, 420, 597